An Integrated Domain Based Evolution Model for the Red Sea: New Seafloor Spreading Evidence

Khamis Farhoud [a,*] and **Ahmed N. El-Barkooky** [b]

[a] KBR, Majnoon Oil Field, Basra, Iraq
[b] Geology Department, Cairo University, Egypt

* Corresponding author: kh_farhoud@hotmail.com
ORCID (corresponding author): https://orcid.org/0009-0004-2675-1686

This is a non-peer-reviewed preprint submitted to EarthArXiv.

This manuscript (version 3) has been submitted for publication in *Heliyon* and is currently under peer review. This version is a revised manuscript prepared in response to reviewer comments; it has not yet been accepted for publication. Subsequent versions of this manuscript may have slightly different content. If accepted, the final version of this manuscript will be available via the "Peer-reviewed Publication DOI" link on the EarthArXiv page for this preprint.

Preprint DOI: https://doi.org/10.31223/X59B5J (version 1 posted February 7, 2026; version 2 posted June 23, 2026; this is version 3, August 2026).

Please feel free to contact the authors; we welcome feedback.

An Integrated Domain Based Evolution Model for the Red Sea: New Seafloor Spreading Evidence

Khamis Farhoud [a]*, Ahmed N. El-Barkooky [b]

Affiliations:

[a] KBR, Majnoon Oil Field, Basra, Iraq.

[b] Geology Department, Cairo University, Egypt.

[a] *Corresponding author Contact.

Email: kh_farhoud@hotmail.com

[b] Co-Author Contact.

Email: abarkook@cu.edu.eg

keywords: Red Sea; Seafloor spreading; Magnetic anomalies; Structural inheritance; Arabian-Nubian Shield; Ocean-continent boundary; Rift evolution.

Abstract

The evolution and lateral extent of oceanic accretion within the central and northern Red Sea remain subjects of long-standing tectonic debate. Although young oceanic crust beneath the southern axial trough is widely accepted, uncertainty persists regarding whether complete separation between the Arabian and Nubian plates has occurred across the basin or whether oceanic crust remains confined to the narrow Median Ridge Valley. This study investigates the crustal architecture of the Red Sea through integrated magnetic, gravity, bathymetric, seismic, and stratigraphic analyses, evaluated with quantitative tests of symmetry, kinematics, and alignment. Organized magnetic anomaly patterns identified in the Central Red Sea indicate a prolonged phase of seafloor spreading: spreading-parallel profile widths of 242 and 212 km, with three modern full rates, bracket accretion between ~10-12 Ma (chron-anchored minimum) and 20.4-24.1 Myr (constant-rate bound), supporting a prolonged pre-evaporite accretion phase. To evaluate this framework independently of magnetic observations alone, regional two-dimensional gravity forward models, lithospheric density, and deep multichannel seismic reflection and refraction data were incorporated, and new mirror-symmetric forward magnetic models (R^2 = 0.86-0.88). The results reveal a basement framework strongly segmented by fault systems associated with the offshore continuation of Precambrian suture zones and the Dead Sea-Aqaba transform system, which control the lateral offset and fragmentation of oceanic domains: the onshore Nakasib and Sol Hamed suture traces project to within 10-13 km of independently mapped offshore magnetic boundaries, and adjacent magnetic stripe groups are offset 49.6 ± 4.8 km across the Atlantis II Transform Fault. Integrated geophysical and stratigraphic evidence suggests the presence of a laterally continuous mafic crustal domain extending up to approximately 125 km from the Median Ridge Valley. These findings imply that the oceanic-continental boundary in the central basin lies close to the present-day coastlines and provide a revised framework for the spatial and temporal evolution of Red Sea rifting.

Introduction

Considerable research has focused on the evolution of the Red Sea and the transition from continental rifting to seafloor spreading. Despite decades of investigation, fundamental questions remain regarding the nature and extent of oceanic crust, the location of the ocean-continent boundary, and the role of Proterozoic structures in controlling rift development. In particular, uncertainty persists as to whether complete separation between the Arabian and Nubian plates has occurred across the basin or whether oceanic crust remains restricted to the narrow axial trough. Recent studies continue to provide contrasting interpretations, with gravity-derived plate reconstructions suggesting significant along-strike variations in crustal architecture [1], while seismic and bathymetric investigations have identified widespread volcanic and neovolcanic features beneath sediment-covered regions, supporting continued oceanic crust formation along large portions of the Red Sea Rift [2]. Furthermore, recent passive seismic observations have revealed active transform faulting and organized tectonic segmentation within the northern Red Sea, indicating mature plate-boundary processes beyond the southern axial trough [3]. To address these issues, the present study integrates magnetic, gravity, bathymetric, seismic, stratigraphic, and geological observations (Fig. 1a-e and Fig. 2) to develop a domain-based model for Red Sea evolution. Interpretations are evaluated against quantitative tests of profile symmetry, new two-dimensional forward modelling, kinematic consistency with published Euler poles, and structural alignment (Figs. 8, 10-13).

1. Relevant Setting and Background

1.1. Early Foundations

Early investigations documented positive gravity anomalies localized along the central of the Red Sea [4,5] and recognized the axial trough as a system of narrow, linear depressions [6]. Subsequent studies explicitly associated this axial region with dense mafic intrusions and deep, segmented troughs (Fig. 1c and d) [7,8], while regional tectonic reconstructions began linking these feature geometries to the large-scale relative motion between the Arabian and African blocks [9,10]. Concurrently, regional marine surveys confirmed the continuity of these central deeps (Fig. 1c) and identified some of the earliest recognized suites of reversely magnetized oceanic rocks in the adjacent Gulf of Aden [11].

1.2. Development of the Seafloor Spreading Hypothesis

A major advance in understanding Red Sea evolution came with the global recognition that linear magnetic anomalies could be directly related to seafloor spreading processes [12]. In parallel, marine seismic refraction lines documented diagnostic lower-crustal velocities between 6.7 and 7.3 km/s beneath the axial trough, accompanied by high-amplitude gravity and magnetic anomalies [13]. Early investigations confirmed that these signatures represented relatively young oceanic crust restricted within the modern axial region [14]. Modern re-evaluations have since refined these subdivisions, contrasting the active axial trough against the distinct structural and volcanic architectures of the marginal zones [15]. Magnetic studies in the late 1960s identified early lineations and high-amplitude anomalies over the axial trough [16], while regional satellite evaluations linked the opening of the main basin to the reactivation of Precambrian structural trends across opposing margins [17]. Subsequent regional potential field mappings further established the continuity of these magnetic fields across the central provinces [18].

1.3. Divergent Views on Crustal Composition

Even with these advances, the crustal configuration of the Red Sea remains controversial. Early kinematic reconstructions utilized rigid plate rotations to model the overall opening of the basin [19], while alternative structural frameworks emphasized the dominant role of attenuated, heavily faulted continental basement along the wide margins [20]. Closer to the subaerial triple junction, structural mapping highlighted the impact of active volcanism along the asymmetric segments of the asymmetric rifts [21], which correlated with the highly fractured basaltic basements sampled at Deep Sea Drilling Project (DSDP) Site 226 [22]. Interpretations of the prominent late Miocene "S" seismic reflector have historically been used to argue for a late, post-evaporitic onset of true seafloor spreading [23]. Conversely, alternative models proposed a multi-stage history involving a much older, pre-Miocene oceanic crust preserved beneath the evaporite [24], highly restricted axial magnetic lineations [25], or broader anomalous dense domains hidden along the margins [26,27].

1.4. Regional Tectonics and Phase Evolution

Regional tectonic evolution is further complicated by the distinct kinematic behavior of the Danakil microplate recognized in regional plate reconstructions [28], multiple distinct phases of crustal development observed in the southern gateways [29], and contrasting crustal thickness interpretations derived from long regional gravity profiles [30]. This structural evolution is widely thought to have advanced via systematic propagating rift segments [31]. To better constrain these variations, structural models have integrated observations from uplifted subaerial mantle exposures such as Zabargad Island [32]. Along the main basin, potential field data and structural variations have been used to subdivide the rift into separate southern, central, and northern provinces [33]. This includes the distinctive transitional domain positioned between 22º N and 25º N, where early studies identified localized oceanization and basaltic emplacements within isolated deeps [34]. Kinematic frameworks have frequently linked this multi-stage tectonic opening directly to the history of the northern Aqaba-Dead Sea strike-slip system [35,36], though alternative models instead postulate a continuous, widespread seafloor spreading history [37]. Nonetheless, debates concerning the exact spatial extent and timing of full oceanization have continued [38], with standard models postulating a youthful axial development [33], an intermediate configuration of continuous accretion since 10-12 Ma flanked by continental shelves [39], contrasted by alternative hypotheses indicating that proto-oceanic magmatic basements developed much earlier beneath the regional Miocene evaporite canopy [24].

1.5. Tectonic Inheritance and Integrated Structural Models

Increasing evidence suggests that inherited lithospheric structures exert a major influence on the segmentation and evolution of the Red Sea rift system. Deep seismic refraction and structural profiles have mapped the extent of extreme crustal thinning and transition zones extending northward toward 26º N [40,41], while detailed investigations of Inter-Trough Zones and transverse elements have attempted to reconcile the contrasting crustal models proposed for the basin [42,43,44,45]. Regional gravity analyses have further demonstrated significant variations in crustal thickness and lithospheric architecture along the Red Sea axis [46]. Within this framework, deep Precambrian structural trends have been interpreted as important tectonic boundaries that directly influenced rift localization and segmentation during subsequent basin evolution. Additional complexity is introduced by the amagmatic structural character of the northern Red Sea province [14], and the substantial influence of Afar-related plume magmatism on the southern sector of the rift system [47,48]. Proposed evolutionary mechanisms include progressive south-to-north rift propagation [49], transtensional deformation associated with rotational oblique extension [50], and locally oblique axial ridge geometries [51].

More recent investigations emphasize the importance of lithospheric inheritance associated with the Arabian-Nubian Shield, where major suture systems may have acted as long-lived lithospheric templates that guided subsequent rift propagation and crustal segmentation [52,53]. Furthermore, the exceptionally thick middle Miocene regional evaporite succession [54] may completely obscure evidence for older oceanic domains beneath the central basin sediment blanket [3,55]. Contemporary seismicity and active volcanism along the margins provide additional insight into ongoing lithospheric processes affecting the broader Red Sea region [56]. Recent geophysical investigations have highlighted substantial along-axis variability in the Red Sea rift system and provided new evidence for active volcanic and magmatic activity beneath these heavily sediment-covered regions of the basin, progressively refining the picture of the extent and distribution of axial oceanic crust [1,2].

The present state of the problem sharpens this debate. Vertical-gravity-gradient mapping places segmented oceanic crust within about 55 km of the shorelines, with spreading initiated by ~13 Ma as an explicit minimum estimate [55]; magnetic-anomaly mapping in the south defines an oceanic domain extending 70-110 km from the axis since ca. 14 Ma [51]; inversion of marine magnetic data places the ocean-continent transition 60-80 km off axis with onset near 10 Ma [61]; and a recent regional synthesis concludes that the northern Red Sea is underlain largely by stretched continental crust while the central basin contains both continental and oceanic domains [1]. Direct seafloor sampling, dated MORB-type gabbros (25 ± 6 Ma), and re-evaluated refraction and satellite-gravity data indicate that oceanic-type accretion begins at depth before continental rupture and that oceanic crust extends tens of kilometres off-axis in the central basin [62-64]. Contrasting kinematic readings of the same magnetic fabric nevertheless persist [50,65], while geodetic kinematics [66] and new seismicity observations [3,67] constrain present-day motion and northern plate-boundary activity. The width, age, and segmentation of the oceanic domain - the questions addressed in this study - therefore remain actively contested.

2. Material and methods

To evaluate contrasting tectonic models of the Red Sea, this study employs a multi-proxy geospatial integration workflow combining gravity, magnetic, seismic, bathymetric, and stratigraphic datasets. These independent datasets were compiled within a unified georeferenced ArcGIS Pro [58] framework to enable consistent spatial comparison and identification of crustal domains across the Red Sea basin.

2.1. Potential Field Analysis

Gravity and magnetic anomaly maps were analyzed to delineate the Median Ridge Valley (MRV) and to identify lateral offsets, linear anomalies, and anomaly terminations (Fig. 3e, f). Magnetic stripes were interpreted following the classical framework of [12], based on two principal characteristics:

1. Linearity of anomalies parallel to the spreading axis.
2. Organized alternation of magnetic polarity.

These features appear as elongated, strike-parallel bands of alternating positive and negative anomalies (dashed white lines, Fig. 3f). In contrast, isolated magmatic intrusions generally produce discrete, high-amplitude circular or irregular anomaly patterns with limited lateral continuity.

Structural lineaments were recognized using several criteria commonly associated with basement discontinuities in potential-field datasets: (1) linear alignment of anomaly gradients on eight potential-field enhancement products, (2) abrupt termination or truncation of anomaly patterns, (3) systematic lateral offsets of magnetic lineations, (4) elongated zones of closely spaced contours indicating steep subsurface gradients, and (5) continuity of these features over regional distances. Where multiple criteria coincided spatially in both magnetic and gravity datasets, the interpreted structures were considered to represent significant crustal boundaries or fault systems rather than local lithological density or susceptibility variations.

Eight potential-field enhancement products were computed from the free-air gravity and total magnetic intensity grids - upward continuation to 5 km, downward continuation to 2 km, and the first vertical derivative of each field, together with the tilt derivative of the gravity field and the analytic signal of the magnetic field (Fig. 4). Structural lineaments were traced along the enhancement-product gradients, which mark the edges of dense and magnetized sources independently of anomaly amplitude; other products served as consistency checks on anomaly continuity and termination. Digitized lineament coordinates, lengths, and azimuths are listed in the supplementary workbook.

2.2. Rationale and Modeling Framework

This study adopts a domain-based interpretation strategy that focuses on anomaly continuity, symmetry, and termination patterns across the basin. The analysis incorporates historical two-dimensional geomagnetic and gravity profiles [15,16,24,30,33,39,46]. These profiles are utilized as mathematically robust reference benchmarks; because the fundamental physical governing equations of gravity and magnetic potential fields have remained invariant, these classical frameworks continue to provide a valid physics-based baseline for modern structural cross-validation. The regenerated profiles shown in Fig. 9 serve as independent geophysical reference models linking observed gravity and magnetic signatures with plausible subsurface source geometries.

Modeling and seismic interpretations (Fig. 9) indicate that magnetized crustal blocks commonly occur between approximately 1.5 and 8 km below sea level, whereas gravity-derived density models consistently identify a relatively dense basement extending beneath much of the Central Red Sea below the evaporite-rich sedimentary succession, whose densities are typically close to 2.2 g/cm^3 [68], as compiled by [61].

These legacy constraints are complemented by new two-dimensional forward magnetic models along profiles A-A′ and B–B′ (Fig. 8). Each model represents the magnetized basement as vertically bounded blocks of alternating polarity within a layer extending 3 km below the basement surface, with a uniform susceptibility of 0.002 cgs; the sedimentary section, including the Miocene evaporites, is treated as non-magnetic. Goodness of fit was quantified by the coefficient of determination (R^2) and the root-mean-square misfit between observed and calculated anomalies. Model geometries and misfit statistics are provided in the supplementary workbook.

2.3. Seismic Velocity Compilation

The use of seismic velocities between 6.4 and 7.0 km/s as indicators of oceanic or intrusive crust is well established in Red Sea geophysics. In particular, the regional refraction datasets [40] documented velocities within this range beneath the evaporite sequence.

A composite seismic refraction profile approximately 1900 km long was reconstructed from VEMA-Atlantis datasets (Fig. 2). Crustal domains were classified according to [33, 39, 40] with values exceeding 6.4 km/s interpreted as oceanic or intrusive crust and velocities below 6.4 km/s interpreted as continental crust; velocities of 6.4-6.7 km/s were not observed in the compiled dataset, so the shield-type and intrusive/oceanic classes are separated by a genuine gap rather than an arbitrarily imposed threshold. The resulting station columns (Fig. 2) are displayed with a vertical exaggeration of approximately 43:1, accompanied by a true-scale companion panel.

2.4. Magnetic Spreading Correlation

A newly interpreted set of magnetic anomalies within the Central Red Sea (white dashed lines in Fig. 3f) was used to estimate the duration of crustal accretion. Thirteen stripe segments were digitized in this study and assigned to five along-axis groups (Fig. 3f); a representative shore-to-shore profile was extracted for each group (Fig. 7), and two profiles, A-A′ and B-B′ (endpoint coordinates in Fig. 6 and the supplementary workbook), were carried through the full width-rate-duration calculation. The along-profile symmetry of each magnetic profile was assessed by mirror-correlation about a sliding trial axis (Figs. 6, 8).

Each measured profile width was projected onto the plate-opening direction predicted at the profile midpoint by the Arabia-Nubia Euler pole of [69], removing the component of profile obliquity. Spreading duration was computed as projected width divided by full spreading rate, using three present-day rate estimates drawn from two independent kinematic solutions: the latitude-interpolated full rates of [70], the rate derived at the profile midpoint from the same Euler pole, and Chu and Gordon’s own best-fitting pole as a cross-check. Present-day rates are taken as representative of the whole spreading history, consistent with the steady state kinematics documented by [66] and the extrapolation argument of [1]. All lengths and azimuths were computed on the WGS84 ellipsoid, with a ±5 km digitization uncertainty assigned to profile endpoints; the complete calculation chain is reproduced in the supplementary workbook.

The resulting age estimates were subsequently compared with independent geophysical observations (Fig. 9a-d), including gravity models suggesting dense mafic crust and seismic reflection and refraction datasets indicating basement continuity beneath the Miocene evaporite succession (Fig. 2; Fig. 9d).

2.5. Bathymetric Analysis

Bathymetric data were analyzed to characterize axial trough morphology, basin segmentation, and depth variations along the Red Sea axis (Fig. 1c, d). These observations were evaluated together with seismic, gravity and magnetic datasets to assess the relationship between seafloor morphology and subsurface geophysical signatures. The operative bathymetric base grid is the satellite-altimetry-derived global topography/bathymetry of the UCSD database (https://topex.ucsd.edu), nominal cell size ~1 arc-minute (~1.8 km), used as delivered (Section 2.8). It was additionally compared with the GMRT v4.5 compilation, in both its blended and multibeam-only (masked) forms, over the Atlantis II corridor (Fig. 12) to document the coverage of verified multibeam soundings within the study area.

2.6. Tectonic Inheritance

Onshore crystalline basement suture zones, including the Nakasib and Sol Hamed sutures (Fig. 1e), were georeferenced and projected offshore to evaluate their spatial relationship with geophysical anomalies and rift segmentation (Figs. 5, 13, 14). This approach allows assessment of tectonic inheritance, whereby pre-existing crustal structures may influence the geometry of modern rifting.

Continuity was tested quantitatively. Each onshore suture trace was projected seaward along its own strike, and the perpendicular (cross-track) distance from the projection to the independently mapped offshore magnetic-zone boundary was computed (Fig. 13); the offshore suture-zone boundaries were digitized from the magnetic data independently of the onshore geology. The likelihood of chance alignment was evaluated against the 15-25°N along-axis search space (1107 km) using a ±25 km acceptance corridor. The same geodesic construction was used to measure the along-transform offset of the Group 1 and Group 2 stripe trends across the Atlantis II Transform Fault (Fig. 12), with uncertainty estimated by ±1.5° perturbation of each trend azimuth. Digitized coordinates are provided in the supplementary workbook. The corridor and search-space definitions are analysis choices; halving the search space doubles the quoted probabilities without changing their order of magnitude.

2.7. Stratigraphic Integration

Chronological reference horizons were used to constrain the timing of the interpreted magnetic sequences (Fig. 3f). These include the Miocene regional marker (~5 Ma) and stratigraphic information from key exploration wells (Fig. 5 for locations). The Jiddah-1 well encountered volcanic sequences within the Eocene interval [57], whereas the Durwara-2 well terminated in basalt at a depth of 4,152 m. In the Maghersum-1 well, the Mukwar Formation (Upper Cretaceous-Paleocene?) rests unconformably on basaltic basement [39], providing an additional stratigraphic constraint on the proposed model.

2.8. Geospatial Integration Framework

All datasets were integrated within a unified georeferenced framework using ArcGIS Pro [58]. This framework ensures spatial consistency among geological, geophysical, bathymetric, and stratigraphic observations and enables systematic evaluation of spatial relationships independent of prior tectonic assumptions (Figs. 1 to 15). Grid resolutions were used as delivered - a nominal cell size of ~5 km for the WDMAM v2.1 magnetic compilation and ~1 arc-minute (~1.8 km) for the satellite-derived gravity and bathymetry grids - and no regridding to finer cell sizes was performed. All lengths, azimuths, and cross-track distances reported in this study were computed on the WGS84 ellipsoid. Dataset sources, native resolutions, and acquisition characteristics are inventoried in the supplementary workbook.

2.9. Kinematic and statistical tests

The azimuth of each digitized structural lineament and magnetic stripe segment was compared with the small-circle direction predicted at its midpoint by published Euler poles (Fig. 11): the Arabia-Nubia pole of [69]; an Arabia–Sinai pole obtained by differencing the Arabia and Sinai angular velocities of [71]; and, for the stripe set specifically — since magnetic stripes record the finite spreading direction most directly — the rotational-transtension prediction of [65], as applied by [50], providing a discriminating test between spreading-parallel kinematics and transtensional shear (results in Section 3.5 and Section 4.4). The angular offset is the acute angle between the observed and predicted axial azimuths. Group-level differences in anomaly-amplitude statistics were evaluated with an exact permutation test over all C(5,2) = 10 possible two-versus-three group splits, and the suture and transform alignment tests use the chance-alignment null of Section 2.6 (Fig. 10). Per-lineament values are listed in the supplementary workbook.

3. Results

3.1. Characterization of Structural Provinces

Integration of georeferenced gravity, magnetic, bathymetric, seismic, and geological datasets delineates three distinct structural provinces and four dominant structural trends within the Red Sea basin.

- **Southern Province (15º 30’N to 20º 30’N)**

  This province is characterized by elongated and laterally continuous magnetic and gravity lineations (Fig. 3e and f). These lineations coincide with a high-amplitude positive gravity anomaly approximately 110 km wide (Fig. 3e), centered on the Median Ridge Valley (MRV). Seismic refraction (Lines 170-178, Fig. 2) record crustal velocities exceeding 6.4 km/s, consistent with well-developed oceanic crust.

- **Central Province (20º 30’N to 23º 30’N).**

  The Central Province is characterized by organized magnetic polarity patterns (Fig. 3f and Fig. 14b). North of the Heya terrane, magnetic anomalies become increasingly decoupled from gravity signatures, where the corresponding gravity anomalies decrease northward across the Nakasib-Heya-Jeddah terrane (Fig. 14a). For axial context, seismic refraction velocities beneath the MRV remain high (6.76-6.97 km/s; Lines 179-181, Fig. 2); independently of the axis, multichannel seismic reflection (location shown in Fig. 5) indicate lateral continuity of high-velocity basement extending tens of kilometers away from the axis (Fig. 9d).

- **Northern Province (23º 30’N to 27º 30’N)**

  Pre-rift stratigraphic units, including the Zabargad Formation, are preserved within this province. Regions adjacent to the coastal margins (Fig. 2 and Fig. 14b for location) exhibit geophysical characteristics compatible with continental basement, supported by seismic refraction velocities below 6.4 km/s. In contrast to the higher-velocity domains identified basin ward, magnetic anomalies are generally weak and discontinuous and lack laterally continuous lineations.

3.2. Identification of Magnetic Stripes and Structural Offsets

Geospatial analysis identifies five groups of linear magnetic anomalies within the Central and Southern provinces (Fig. 3f). These anomalies are characterized by strike-parallel continuity and lengths ranging from approximately 70 to 190 km. Group 5 is comparatively more fragmented, with lineations segmented by small-scale strike-slip structures (Fig. 3f). The geometry and continuity of these anomalies are consistent with organized spreading-related patterns rather than isolated continental intrusions.

A major structural discontinuity occurs near Atlantis II Deep at approximately 20º 30’N. The gravity anomaly terminates abruptly at this latitude (Fig. 3e), and the trends of the Group 1 and Group 2 magnetic stripes intersect the mapped Atlantis II Transform Fault at crossing points separated by 49.6 ± 4.8 km along the transform trace (Fig. 12). The offshore trace of the Nakasib suture meets the same transform trace within 0.30 km (chance-alignment $p \approx 0.001$; Fig. 10g), while the Sol Hamed suture, unrelated to the Atlantis II Transform Fault, lies 105 km from its own independently mapped target, the northern limit of coherent lineations, far outside the acceptance corridor, and is plotted on the same panel as a negative control (Fig. 10g). Within this corridor, the multibeam-only (masked) GMRT v4.5 grid contains no data over 90% of the area (Fig. 12c). The stated ±4.8 km reflects stripe-azimuth uncertainty only.

3.3. Amplitude Statistics and Along-Axis Variations

The anomaly-amplitude distributions of the five stripe groups overlap substantially (Fig. 10a-c). The exact permutation test over all ten two-versus-three group splits detects no statistically significant separation in any of the six summary statistics (minimum $p = 0.20$ against a minimum attainable p of 0.10; Fig. 10f; per-group statistics in the supplementary workbook). Along-axis trends of gravity-high width and magnetic-anomaly width are shown in Fig. 10d-e. The continuity of the linear anomaly patterns becomes increasingly disrupted southward by strike-slip offsets associated with transform faults and Precambrian structures, including the Nakasib suture zones (Figs. 3f).

3.4. Stratigraphic Constraints and Magnetic Correlation

Seismic refraction measurements acquired near the eastern termination of profile A-A’ (Lines 180-181; Fig. 2 and Fig. 5) reveal crustal velocities reaching approximately 6.97 km/s within the deeper basement interval. These velocity values correspond closely with the high-velocity basement unit recognized on previously published seismic interpretations (Fig. 2). In addition, multichannel seismic reflection profiles (Fig. 9d) demonstrate that this basement package extends laterally for nearly 80 km on both sides of the present-day axial trough.

Additional constraints are provided by exploration well information and regional stratigraphic markers (Fig. 5 for location). The available subsurface observations are compatible with the presence of an older mafic basement underlying the central basin. These well penetrations constrain the minimum age of the volcanic basement rather than its oceanic versus continental affinity.

The magnetic anomalies interpreted in this study (white dashed lineations in Fig. 3f) form an organized sequence of alternating polarity patterns extending for approximately 250 km across the Central Red Sea beneath the regional Miocene horizon. Profile A-A′ spans 259.6 km shore-to-shore (N61.0°E), corresponding to a projected spreading-parallel width of 242.4 km; profile B-B′ spans 226.7 km (211.7 km projected). The best-fit magnetic symmetry axis on A-A′ lies at 115 km ($r = 0.68$; Fig. 6) and the forward-model axis at 124 km (Fig. 8); both lie within 15 km of the 129.8 km geodetic midpoint. The two-dimensional forward models reproduce the observed anomalies with $R^2 = 0.86$ (RMS misfit 41.8 nT) on A-A′ and $R^2 = 0.88$ (RMS 32.1 nT) on B-B′ (Fig. 8). At the three full-rate estimates of Section 2.4 (10.0-12.4 mm yr^{-1} at the profile latitudes), the projected widths yield spreading durations of 17.1-20.1 Myr for B-B′ and 20.4-24.1 Myr (median 20.6 Myr) for A-A′

3.5. Dominant Structural Trends

Four principal structural trends were identified through integrated interpretation of magnetic and gravity anomaly patterns and comparison with established regional tectonic fabrics (Fig. 3; identification criteria in Section 2.1).

- **N-S basement lineaments (Fig. 3a):** expressed as long, linear gravity and magnetic gradients interpreted as deep-seated basement faults that parallel the principal Red Sea rift orientation.
- **Suture-related trends (Fig. 3b):** represented by abrupt terminations of gravity anomalies and changes in magnetic fabric that coincide with the offshore projection of major Arabian-Nubian Shield terrane boundaries, including the Nakasib suture system.
- **NW-SE oblique fabrics (Fig. 3c):** identified from oblique magnetic lineaments trending approximately 114-123°.
- **NE-SW strike-slip structures (Fig. 3d):** characterized by systematic lateral displacement of magnetic lineations and local segmentation of anomaly belts. These structures are interpreted to reflect transform-related deformation associated with the Aqaba-Dead Sea fault system. The Atlantis II and Mabahiss transform zones represent prominent examples of this structural trend.

The azimuthal distribution of each trend is summarized as rose diagrams (Fig. 6b for the four structural trends; Fig. 6c and Fig. 11a for the five magnetic stripe groups). The small-circle test of Section 2.9 (Fig. 11) yields mean angular offsets from the Nubia-Arabia pole prediction of 39.5° for the N-S basement lineaments ($n = 6$), 9.9° for the suture-related trends ($n = 5$), 75.4° for the NW-SE oblique fabrics ($n = 8$), and 22.4° for the Aqaba-Dead Sea set ($n = 9$). Against the Arabia-Sinai pole, the mean offset of the Aqaba-Dead Sea set falls from 22.4° to 5.1°, improving the fit on all nine lineaments (Fig. 11d). For the thirteen magnetic stripe segments, the spreading-parallel prediction gives a mean offset of 8.8°, closer than the rotational-transtension prediction (81.7°) for all thirteen segments (per-lineament values in the supplementary workbook).

3.6. Onshore-Offshore Suture Continuity

The seaward projections of the onshore Sol Hamed and Nakasib suture traces fall 13.2 km and 10.4 km, respectively, from the independently mapped bottom boundary of the corresponding offshore magnetic suture zones, whose full widths are 91.3 ± 9.4 km (Sol Hamed) and 94.6 ± 2.4 km (Nakasib) (Fig. 13). Against the 15-25°N search space (1107 km) with a ±25 km acceptance corridor, the corresponding chance-alignment probabilities are $p = 0.024$ and $p = 0.019$ (corridor prior $p = 0.045$; Fig. 13c; individual width estimates in the supplementary workbook). The projections align in position; the offshore zone azimuths differ from the onshore trace azimuths (Fig. 13), as expected where the offshore boundaries follow the magnetic fabric of the suture zones rather than the strike of the projected trace, the test is positional, not directional. Four alignment tests are reported in total; under a conservative Bonferroni correction the Nakasib-transform result ($p \approx 0.001$) remains significant, while the two suture-boundary alignments become individually marginal and are interpreted as mutually corroborating.

4. Discussion

The tectonic interpretation proposed in this study is derived from an integrated geospatial framework that combines the continuity of potential-field anomalies, their lateral terminations, and their geometric relationships across the basin. Previously published gravity and magnetic models (Fig. 9) were used as independent geophysical constraints for evaluating the distribution of crustal domains within the Red Sea. By integrating these regional datasets (Fig. 9a-d) with the anomaly patterns identified in the present study (Figs. 3 and 14), a unified framework is developed for examining the spatial distribution, structural organization, and temporal evolution of the basin. Emphasis is placed on observations that discriminate between competing interpretations, supported by quantitative tests of profile symmetry, kinematic consistency, and structural alignment (Figs. 8, 10, 11, 13).

4.1. The Southern Red Sea Province

The southern Red Sea is dominated by a narrow axial depression composed of relatively straight and steep-sided bathymetric troughs that define the present-day spreading axis (Fig. 1d; Fig.7). Earlier interpretations proposed that oceanic crust occupied much of the basin and that oceanization may have initiated as early as approximately 40 Ma [24][.]{.mark} However, preservation of older sedimentary sequences along the basin margins is difficult to reconcile with such widespread early oceanization. The integrated gravity and magnetic datasets analyzed in this study instead suggest that the thickest and densest magmatic crust is concentrated within the Median Ridge Valley (MRV), where it forms a continuous axial belt approximately 110 km wide (Fig. 3e).

This oceanic domain can be traced northward along the principal rift axis before terminating near 20º 30′N in the vicinity of the offshore extension of the Nakasib suture and the Atlantis II Transform Fault (Fig. 3e; Fig. 12). The geometry of the potential-field anomalies further suggests that crustal accretion within the southern province is strongly influenced by NE-SW strike-slip deformation (Fig.3f). These structures offset and segment magnetic Groups 3, 4, and 5 (Fig. 3f), implying that inherited basement fabrics continue to exert an influence on the segmentation and geometry of the active spreading system.

4.2. The Central Red Sea: Evidence for a Prolonged, Pre-Evaporite Spreading History

Within the Central Red Sea, the combined geophysical observations support a domain-based evolutionary model involving an early stage of oceanic crust generation. Organized linear magnetic anomalies identified within Group 1 (Fig. 3f and Fig. 14b) occur beneath the regional Miocene reflector imaged on seismic data (Fig. 9d), indicating that the interpreted crustal accretion predates deposition of the evaporite succession. The computed spreading durations of 20.4-24.1 Myr for profile A-A′ and 17.1-20.1 Myr for B-B′ (Section 3.4) indicate that oceanic accretion in the Central Red Sea began substantially earlier, and occupied a broader area, than in models that restrict oceanization to the young 2-3 Ma axial spreading cells. This result independently supports earlier proposals of a pre-Miocene accretion phase [37].

These durations are compatible with, rather than contradicted by, recent age estimates of ca. 13-14 Ma. The ~13 Ma of [55] is described by those authors as "only a minimum estimate", with the explicit caveat that seafloor spreading could have started earlier; and the ca. 14 Ma of [51] is reproduced by the same rate arithmetic applied to their narrower interpreted domain, so that the difference between the age estimates reduces to a difference of roughly 30 km per flank in interpreted domain width. On spatial extent, the ~125 km half-width interpreted here lies between the 70-110 km of [51] and the near-coastline extent mapped by [55], with the 60-80 km of [61] and the mid-basin estimate of [1] bracketing it from below.

Direct sampling and geophysical surveying of the Thetis and Nereus cells (Fig.1 c; Fig.14a) documented an initial burst of rapid oceanic accretion at the onset of each spreading cell, fading into slower steady-state accretion as the rift widens [62]. Such cell-by-cell initiation is consistent with the diachronous, domain-based development inferred here, in which different sectors of the basin entered the accretion stage at different times. MORB-type melt intrusions preceded continental rupture in the northern Red Sea, with a gabbro dated at 25 ± 6 Ma ($^{40}Ar/^{39}Ar$) recording intrusion during early rifting [63], radiometric evidence that oceanic-type magmatism begins at depth well before full rupture, and an age bracket compatible with the 20.4-24.1 Myr accretion durations computed here.

This duration assumes a constant, present-day spreading rate; if accretion instead followed the burst-then-steady-state pattern at the Thetis and Nereus cells [62], early faster rates would make the true duration shorter than this estimate. Izzeldin's [39] independently chron-anchored correlation dates continuous accretion in this sector to 10-12 Ma, taken here as a lower bound consistent with that bias.

The axial deeps of the Red Sea provide an independent check on this domain framework. In the north, the Thetis and Nereus Deeps mark the youngest, most recently initiated spreading cells [62], consistent with their position outboard of the older central domain proposed here. In the central Red Sea, the Atlantis II and Hatiba Deeps define a comparably young, still-forming transition zone within the same corridor [33], matching the modeled axis rather than displacing it. This spatial coincidence is corroborating rather than circular: bathymetric deeps were not among the criteria used to define the domain boundaries in Section 2.1.

Although these estimates vary according to the selected kinematic parameters, the principal geological interpretation remains unchanged. All tested scenarios imply crustal accretion that significantly predates the approximately 5 Ma Miocene marker horizon and therefore support the existence of an older spreading phase within the Central Red Sea. Accordingly, the proposed framework is not dependent upon a single spreading solution but remains robust across the realistic range of modern full-rate estimates (Section 2.4).

Independent seismic observations are consistent with this interpretation. Seismic investigations [39,40] reported basement velocities between 6.5 and 6.9 km/s beneath regionally continuous acoustic basement units (Fig. 2). Likewise, multichannel seismic reflection profiles (Fig. 9d) indicate that this basement horizon extends laterally away from the present axial zone toward the basin margins. Earlier refraction surveys documented similar velocity ranges of approximately 6.6-7.3 km/s within laterally persistent crustal layers [15], values commonly interpreted as representative of oceanic Layer 3 or mafic intrusive crust. A re-evaluation of the refraction data east of Thetis Deep, combined with satellite-derived gravity, reached the same conclusion independently: gabbroic velocities of 6.6-6.9 km s^{-1} extend to 65 km from the axis, and paired gravity trends resembling oceanic fracture zones support oceanic rather than extended continental crust in this part of the central Red Sea [64].

Additional support is provided by regional gravity observations. The long regional profiles [30], extending for more than 1500 km across the basin (Fig. 9b), are characterized by a broad Bouguer gravity high exceeding +100 mGal within the central basin. Forward modelling of these anomalies requires relatively dense crustal material with densities between approximately 2.90 and 3.00 g/cm^3 replacing continental crust with densities of approximately 2.67-2.80 g/cm^3 (upper-crustal values; whole-crust shield averages are near 2.85 g/cm^3, Fig. 9). The interpreted magnetic domain identified in this study, extending for nearly 250 km across the basin (white dashed boundaries in Fig. 14b), closely coincides with this region of elevated crustal density.

The reconstructed lithospheric architecture shown in Figs. 9 further indicates progressive crustal attenuation toward the rift axis. Outside the basin, the Afro-Arabian Shield retains a typical continental crustal configuration with average crustal densities of approximately 2.85 g/cm^3 overlying mantle material with densities near 3.35 g/cm^3. Beneath the Central Red Sea, however, gravity models indicate Moho depths of approximately 11 km together with crustal densities approaching 2.88 g/cm^3, underlain by anomalously low-density uppermost mantle (3.25 g/cm^3, Fig. 9b) relative to the 3.35 g/cm^3 shield mantle beneath Miocene and Plio-Pleistocene sedimentary packages.

The thick Miocene evaporite succession described by [39] may conceal evidence of earlier spreading episodes by obscuring the geometry of the underlying basement surface. Consistent with this, [61] showed that subdued off-axis anomaly amplitudes are quantitatively explained by isostatic depression of the magnetized basement beneath the evaporite load, magnetizations remaining significant even where the basement lies several kilometres below the salt. Lateral flowage can also emplace Miocene evaporites over younger crust, but the described flow features are confined to the walls of the axial trough [72,73], well inside the more than 100-km-wide domain considered here. Nevertheless, multichannel seismic reflection data continue to image laterally continuous basement beneath the salt layer (Fig. 9d), suggesting that the mafic crustal domain extends well beyond the present Median Ridge Valley. Collectively, the seismic observations, gravity-derived density distributions, and basin geometry are compatible with a laterally extensive mafic crustal province and imply that the ocean-continent boundary may occur considerably closer to the present coastlines than proposed by models restricting oceanization to the modern axial trough. Regional allochthonous salt movement could in principle decouple suprasalt structure from basement fabric; the lineaments interpreted here, however, are expressed in potential-field data that sense the basement beneath the salt rather than the salt surface.

The geometry of the magnetic anomalies themselves favors sustained crustal accretion rather than isolated volcanic centers. Magnetic maps together with profile A-A' (Figs. 6, 14b) reveal a central positive anomaly bordered by repeated sequences of alternating positive and negative anomalies that display broad cross-axis symmetry. Such patterns resemble the magnetic fabric typically associated with prolonged seafloor spreading. The two-dimensional forward models reproduce this organization with mirror-symmetric polarity blocks ($R^2 = 0.86$ and 0.88; Fig. 8), and the two independent axis determinations (115 km correlation-based, 124 km forward-model; Figs. 6, 8) lie within 15 km and 6 km of the geodetic midpoint.

Further age constraints are provided by exploration wells shown in Fig. 5. Evidence from the Maghersum, Durwara, and Jiddah wells [39,57] documents the presence of pre-Miocene stratigraphic intervals above the interpreted basement surface, indicating that mafic basement formation predates the Pliocene sedimentary succession. Additional support is provided by the character of profile A-A' (Fig. 6), where long-wavelength and relatively low-frequency magnetic variations contrast with the short-wavelength anomaly patterns typically associated with narrow and recently active spreading centers.

Finally, the observed differences in polarity and amplitude between the northern and southern magnetic groups are qualitative: the amplitude statistics of the five groups are not statistically separable at this sample size (minimum $p = 0.20$ against a minimum attainable p of 0.10, so this null result is weak evidence; Fig. 10f). These differences may reflect variations in spreading history, fault segmentation, magmatic supply, or later tectonic modification associated with inherited structures and transform deformation. The pronounced structural segmentation affecting the southern sector may therefore contribute to reduced magnetic amplitudes independent of the degree of present-day magmatic activity.

4.3. The Northern Red Sea Province

In contrast to the stronger magmatic and potential-field signatures observed farther south, the northern Red Sea displays geophysical characteristics more compatible with continental extension than with mature seafloor spreading. The preservation of pre-rift sedimentary successions on Zabargad Island (location shown in Fig. 14b), together with seismic refraction velocities generally lower than 6.4 km/s near the basin margins (Fig. 2), supports the persistence of attenuated continental crust beneath much of the northern province, in agreement with the recent synthesis of [1], which concludes that the northern Red Sea is underlain largely by stretched continental crust.

Potential-field anomalies north of the Sol Hamed suture system (Fig. 3e and Fig. 14b) are comparatively weak, irregular, and lack the long, strike-parallel continuity observed within the central and southern sectors. Such anomaly patterns are more compatible with distributed extension, block faulting, and heterogeneous basement architecture than with laterally organized oceanic accretion. Active spreading-related and transform seismicity is nevertheless documented in the northern province [3,67], indicating a tectonically active, if structurally immature, plate boundary. Basalts recovered from the northern axial deeps, including Shaban and Mabahiss, are moreover of MORB affinity without geochemical evidence of continental contamination [76,77], demonstrating that focused oceanic-type magmatism is already active within these localized nascent cells; the dominantly continental character inferred here therefore applies to the broad off-axis region between the deeps, not to the axial deeps themselves. Collectively, these observations suggest that the northern Red Sea remains dominated by stretched continental lithosphere and represents the least mature stage of basin evolution among the three provinces identified in this study.

4.4. Structural Control: Suture Zones and Tectonic Inheritance

The spatial arrangement of the structural provinces defined in this study appears closely linked to the geometry of major Arabian-Nubian Shield sutures, which may have influenced both the extent and segmentation of magmatic accretion. In particular, the Nakasib suture system forms a major crustal boundary separating the actively spreading southern province from the older crustal domain interpreted within the central Red Sea (Fig. 3e-f), independently corroborated by the derivative and enhancement products of Fig. 4.

A prominent example of this structural influence is the 49.6 ± 4.8 km lateral offset between the Group 1 and Group 2 stripe trends across the Atlantis II Transform Fault (Fig. 12). The offshore trace of the Nakasib suture meets the same transform within 0.30 km of this crossing region (Fig. 10g), an alignment whose chance probability within the mapped lineation province is small (Fig. 10g), suggesting that inherited basement fabrics guided rift localization and controlled the segmentation of the evolving spreading center.

Farther north, the Sol Hamed suture appears to define the northern limit of coherent magnetic lineations and organized spreading-related anomalies (Figs. 3b, 3f, and Fig. 14). Across this boundary, the relatively continuous anomaly fabric of the central province transitions progressively into the discontinuous and lower-amplitude signatures (Fig. 14b).

The continuity of both sutures across the shoreline is quantitatively supported: the onshore Sol Hamed and Nakasib traces project seaward to within 13.2 km and 10.4 km of the independently mapped boundaries of the offshore magnetic suture zones ($p = 0.024$ and $p = 0.019$; Fig. 13). Alignment between onshore sutures and offshore magnetic boundaries has not previously been evaluated quantitatively in this basin, and proximity-based association has been noted as difficult to test [1]. The inference of inherited structural control is consistent with the proposal of [51] that Red Sea rift segmentation reflects continental transfer zones influenced by NNE-trending Proterozoic shear zones and sutures. It is complementary to, rather than in conflict with, the onshore coastline-offset analysis of [1]: that test addresses permanent lateral offset of the margins, whereas the present test addresses the position of offshore magnetic boundaries relative to projected suture traces. A gravity-based analysis independently linked short-offset spreading-segment discontinuities to paired shield sutures, including the Nakasib [74], supporting suture control on offshore segmentation; the present test addresses a different offshore element (the magnetic suture-zone boundaries) and is complementary.

Taken together, these observations suggest that the inherited architecture of the Arabian-Nubian Shield exerted a control on Red Sea development. Within this framework, three principal evolutionary domains are recognized (Fig. 14c):

Southern Province (Fig. 3e-f): active axial spreading concentrated within the Median Ridge Valley and modified by transform segmentation.

Central Province (Fig. 3f; Fig. 14b): an older mafic or oceanic domain recording a prolonged history of crustal accretion beneath the Miocene evaporites, with computed accretion durations of 20.4-24.1 Myr (Section 3.4).

Northern Province (Fig. 14b): a dominantly continental rift system characterized by diffuse extension and strong inheritance from Neoproterozoic basement structures and the Aqaba-Dead Sea transform system.

4.5. Alternative Explanations for the Central Red Sea Magnetic Anomalies

Interpretation of magnetic anomalies is inherently ambiguous, and alternative explanations for the anomaly patterns identified in the central Red Sea including isolated intrusions, volcanic complexes, and structurally controlled basement highs must therefore be considered alongside any spreading-related interpretation.

The most substantive alternative is that of [39], who modelled the off-axis anomalies at 19-22°N with basalt-capped, tilted continental fault blocks of fit comparable to oceanic models, and described the off-axis zone as magnetically quiet. Three considerations bear on this alternative.

First, that study's own preferred interpretation places oceanic crust roughly 80 km either side of the axis with continuous accretion since 10-12 Ma, closer to the present model than to axial-trough-only interpretations. Second, the subdued off-axis amplitudes are quantitatively accounted for by isostatic depression of the magnetized basement beneath the evaporite load [61], without requiring the absence of oceanic crust.

Third, the organization requirement was tested directly with new forward models (Fig. 15), built with the same basement geometry, 3-km layer thickness, and field parameters as the Fig. 8 spreading model, so only the magnetization pattern differs between models. Two continental alternatives were tested. A uniform layer magnetized only by induction from the present-day field does not fit at all ($R^2 = 0.01$). Fault blocks 10-20 km wide, the scale typical of rifted-margin blocks, carrying a single polarity fit poorly ($R^2 = 0.69$). The same blocks given random, unorganized polarities also fail: a typical random trial reaches only $R^2 = 0.09$, and even the best of 3,000 random trials reaches only $R^2 = 0.83$, short of the spreading model's $R^2 = 0.86$, and reachable by chance less than 3 times in 10,000 ($P < 0.0003$) (Fig. 15a). Adding eight discrete mafic intrusions to the same continental background (Fig. 15b) improves the fit to $R^2 = 0.70$, but the intrusions cluster near the axis and still fail to reproduce the flanking alternation.

Fit quality rises step by step with how much of the organized, reversal-driven spreading pattern is built into the model, from $R^2 = 0.01$ (continental, no structure) to 0.70 (discrete intrusions) to 0.86 (full reversal-organized accretion; Fig. 15c). A freely tuned magnetization can match the spreading model's fit (0.86 versus 0.86), consistent with the fit-equivalence reported by [39], but matching it requires reproducing the same alternating, reversal-organized pattern that seafloor spreading predicts as a physical consequence of polarity reversals during accretion (full model definitions and fit statistics in the supplementary workbook).

Because potential-field forward models are inherently non-unique, the seismic depth-section evidence in Fig. 9d provides a more direct constraint: Izzeldin's [39] seismically-determined basement configuration places oceanic crust up to 80 km from the axis in the southern profiles, independent of the alternating-polarity magnetic modelling discussed above. A recent interpretation attributes subdued anomalies to distributed mafic intrusion into thinning continental crust, delaying spreading onset to ~5 Ma [75]. The alternating-polarity organization, axial symmetry, and Euler-pole-parallel azimuths documented here (Figs. 6, 8, 11) are collective properties that distributed intrusion does not readily predict, although the two mechanisms may coexist along strike.

A second alternative interprets much of the same magnetic fabric as transtensional basement structure rather than spreading-related lineation, and reports no evidence for oceanic crust beneath the sedimentary cover [50]. The kinematic test of Section 3.5 addresses this reading directly: the axial azimuths of all thirteen stripe segments lie closer to the spreading-parallel prediction (mean offset 8.8°) than to the rotational-transtension prediction (81.7°; Fig. 11), and the mirror-symmetric organization of the profiles (Figs. 6, 8) is characteristic of accretion rather than distributed shear.

Several observations further favor a model involving regionally organized crustal development. The anomalies display elongated strike-parallel geometries, repeated polarity changes, and systematic offsets that coincide spatially with transform structures and with the offshore projections of major Arabian-Nubian Shield sutures (Figs. 3f and 14a). Such spatial organization is difficult to explain solely through isolated volcanic centers or local intrusive bodies.

Additional support comes from independent geophysical datasets. Seismic refraction studies report crustal velocities exceeding 6.4 km/s [15,39,40], while multichannel seismic profiles reveal regionally continuous basement beneath the Miocene evaporite cover (Fig. 9d). Similarly, multiple gravity investigations conducted over several decades (Fig. 9) consistently identify a broad high-density central corridor associated with crustal thinning, Moho uplift, and long-wavelength positive gravity anomalies.

Although alternative interpretations cannot be completely excluded, the combined magnetic, seismic, gravity, and stratigraphic evidence favors the presence of a laterally extensive mafic crustal domain rather than isolated volcanic centers alone. Within this interpretation, Red Sea evolution appears to reflect not only rift-related magmatism but also the strong influence of inherited lithospheric structures derived from the Arabian-Nubian Shield. A chron-tied reversal sequence from modern aeromagnetic acquisition, or deep-penetration scientific drilling, data types not yet acquired in this sector, would provide direct tests of the geometry, symmetry, and timing of this proposed early spreading phase.

4.6. Limitations

Three limitations bound these results. First, the duration estimates assume constant full rates; the chron-anchored 10-12 Ma minimum [39] and the burst-then-steady-state kinematics of [62] bracket the effect of that assumption (Section 4.2). Second, potential-field forward models are non-unique, and the seismic constraints of Fig. 9d are therefore treated as the primary off-axis evidence, and the fit-equivalence of non-spreading models is quantified directly in Section 4.5 (Fig. 15). Third, grid resolution (~5 km horizontal sampling for the magnetic compilation) and the limited verified bathymetry near the Atlantis II corridor (Fig. 12c) limit positional precision; this horizontal sampling is a separate quantity from the 3-km vertical layer thickness used in the forward models of Section 2.2, and is not constrained by the magnetic grid's cell size. A chron-tied reversal sequence from modern aeromagnetic data, or deep-penetration drilling, would directly test the proposed early accretion phase.

Conclusion

This study develops an integrated geospatial framework to investigate the crustal architecture and tectonic evolution of the Red Sea using gravity, magnetic, seismic, bathymetric, and stratigraphic datasets. Combining these independent observations within a common spatial geo-reference system reveals three major structural provinces whose distribution closely follows inherited Arabian-Nubian Shield basement fabrics and major suture zones.

The southern Red Sea is characterized by active oceanic accretion concentrated within a relatively narrow axial corridor approximately 110 km wide. This spreading system extends northward along the Median Ridge Valley before terminating near 20º 30'N in the vicinity of the offshore continuation of the Nakasib suture and the Atlantis II Transform Fault.

Farther north, the Central Red Sea contains evidence for a broad mafic crustal domain extending approximately 125 km away from the present-day spreading axis. Organized magnetic lineations, high seismic velocities, gravity-derived crustal densities, and stratigraphic relationships beneath the Miocene evaporite sequence collectively support the existence of an earlier phase of crustal accretion that persisted for at least ~10-12 Myr and up to 20-24 Myr (constant-rate bound) during the early stages of basin development.

North of the Sol Hamed structural boundary, geophysical observations become progressively more consistent with continental extension rather than mature oceanic spreading. This northern province is characterized by weaker and less continuous potential-field anomalies, distributed deformation, and seismic velocities typical of stretched continental crust.

Taken together, the observations presented here indicate that Red Sea evolution was neither spatially uniform nor temporally synchronous along strike. Instead, the basin appears to have evolved through a series of structurally controlled domains in which inherited Neoproterozoic basement fabrics and transform-related deformation strongly influenced the location, geometry, and segmentation of the rift through time. The offshore continuations of the Nakasib and Sol Hamed sutures align with independently mapped magnetic boundaries at the few-kilometre level, and the suture-related structural trend is kinematically consistent with the Nubia-Arabia opening direction, providing a quantitative basis for this structural inheritance.

Authorship contribution statement

Khamis Farhoud: Conceptualization, Data curation, Formal analysis, Methodology, Project administration, Software

Supervision, Validation, Visualization, Writing - original draft, Writing - review & editing.

Ahmed N. El-Barkooky: Conceptualization, Data curation, Formal analysis, Investigation, Methodology, Project administration, Resources, Supervision, Validation, Visualization, Writing - original draft, Writing - review & editing.

Funding

This research did not receive any specific grant from any source.

Declarations

Ethics declaration

This study did not involve human participants, human data or tissue, or animals, and no ethical approval was required. All datasets analyzed are publicly available or compiled from the published literature, as described in the Data availability statement.

Declaration of competing interest

The authors declare that they have no known competing financial interests or personal relationships that could have appeared to influence the work reported in this paper.

Data availability

Data included in the article/supplementary material is referenced in the article. All data associated with this study are provided as Supplementary Material submitted with the manuscript: a consolidated supplementary workbook (all digitized lineament, stripe, suture, and profile coordinates; derived geometry; kinematic tests; and calculation chains) together with exports of every digitized feature. The underlying regional grids are publicly available from the NOAA National Centers for Environmental Information (https://www.ngdc.noaa.gov), the UCSD Topographic/Bathymetric database (https://topex.ucsd.edu), the World Digital Magnetic Anomaly Map repository (http://www.wdmam.org), and the GMRT synthesis (https://www.gmrt.org).

Preprint Disclosure

A prior version of this manuscript has been deposited as a preprint on EarthArXiv on February 7, 2026 (Updated June 23, 2026) and can be accessed at https://doi.org/10.31223/X59B5J.

Acknowledgements

We express our sincere gratitude to Mr. Dia Mahmoud (GEOPEX Ltd.) and Dr. Hussein Hammouda (Former Chairman of the Egyptian Mineral Resources Authority) for their invaluable assistance in digitizing the historical Red Sea magnetic and gravity paper sheets. Special thanks are extended to the late Dr. Wafik Mishrif for his foundational support and encouragement during the collection of the magnetic and gravity datasets across the Gulf of Suez and the Red Sea. We are grateful to the National Geophysical Data Center (NGDC) for providing access to the gravity and magnetic data acquired over the Red Sea region. We also wish to thank Dr. Hans A. Roeser for generously sharing his original gravity and magnetic materials from 1975, 1976, and 1980.

References

[1] N.C. Mitchell, A.Y. Izzeldin, I.C.F. Stewart, Nubia-Arabia separation: Clues from oceanic spreading fabric in the Red Sea, Gondwana Res. 147 (2025) 301-320. https://doi.org/10.1016/j.gr.2025.06.019.

[2] J. Preine, N. Augustin, N.C. Mitchell, F.M. van der Zwan, A.-C. Wölfl, M. Schade, Y.A. Izzeldin, M.A.M. Osman, C. Hübscher, Tracing the Neovolcanic zone along the sediment-covered

regions of the Red Sea Rift, Sci. Rep. 15 (2025) 5481. https://doi.org/10.1038/s41598-025-89332-2.

[3] H.A. Shiddiqi, L. Parisi, E. Valero Cano, M. Fittipaldi, N. Augustin, G. Baby, P.M. Mai, S. Jónsson, Transform faulting in the Northern Red Sea revealed by ocean bottom seismometers deployed in the Zabargad Fracture Zone, Geochem. Geophys. Geosyst. 26 (2025) e2025GC012253. https://doi.org/10.1029/2025GC012253.

[4] F.A. Vening Meinesz, Gravity Expeditions at Sea, 1923–1932, Vol. II, Netherlands Geodetic Commission, Delft, 1934. https://doi.org/10.54419/3us2nj.

[5] A.E. Von Triulzi, Expedition S.M. Schiff "Pola" in das Rothe Meer nördliche Hälfte (1895/1896). Relative Schwerebestimmungen, Denkschr. Akad. Wiss. Wien Math.-Nat. Kl. 65 (1898) 131.

[6] L. Owen, Origin of the Red Sea depression, AAPG Bull. 22 (1938) 1217–1223. https://doi.org/10.1306/3d932fe0-16b1-11d7-8645000102c1865d.

[7] R.W. Girdler, The relationship of the Red Sea to the East African Rift System, Q. J. Geol. Soc. Lond. 114 (1958) 79-105. https://doi.org/10.1144/gsjgs.114.1.0079.

[8] H. Tazieff, Une récente campagne océanographique dans la mer Rouge, Bull. Soc. Belge Geol. 61 (1952) 84-90.

[9] S.W. Carey, A tectonic approach to continental drift, in: Continental Drift: A Symposium, University of Tasmania, Hobart, 1958, pp. 177-355.

[10] A.M. Quennell, Tectonics of the Dead Sea rift, in: Proc. 20th Int. Geol. Congr., Mexico City, 1956, pp. 385-405.

[11] R.W. Girdler, G. Peter, An example of the importance of natural remanent magnetization in the interpretation of magnetic anomalies, Geophys. Prospect. 8 (1960) 474-483. https://doi.org/10.1111/j.1365-2478.1960.tb01730.x.

[12] F.J. Vine, D.H. Matthews, Magnetic anomalies over ocean ridges, Nature 199 (1963) 947-949. https://doi.org/10.1038/199947a0.

[13] C.L. Drake, R.W. Girdler, A geophysical study of the Red Sea, Geophys. J. 8 (1964) 473-495. https://doi.org/10.1111/j.1365-246X.1964.tb06303.x.

[14] C. Tramontini, D. Davies, Seismic refraction survey in the Red Sea, Geophys. J. 17 (1969) 225-241. https://doi.org/10.1111/j.1365-246x.1969.tb02323.x.

[15] J.R. Cochran, Northern Red Sea: Nucleation of an oceanic spreading center within a continental rift, Geochem. Geophys. Geosyst. 6 (2005) Q03006. https://doi.org/10.1029/2004gc000826.

[16] J.D. Phillips, J. Woodside, C.O. Bowin, Magnetic and gravity anomalies in the central Red Sea, in: E.T. Degens, D.A. Ross (Eds.), Hot Brines and Recent Heavy Metal Deposits in the Red Sea, Springer, Berlin, 1969, pp. 98-113. https://doi.org/10.1007/978-3-662-28603-6_10.

[17] M. Abdel-Gawad, Geological structures of the Red Sea area inferred from satellite pictures, in: E.T. Degens, D.A. Ross (Eds.), Hot Brines and Recent Heavy Metal Deposits in the Red Sea, Springer, Berlin, 1969, pp. 25-37. https://doi.org/10.1007/978-3-662-28603-6_5.

[18] T.D. Allan, Magnetic and gravity fields over the Red Sea, Philos. Trans. R. Soc. Lond. A 261 (1970) 153–180. https://doi.org/10.1098/rsta.1970.0030.

[19] D.P. McKenzie, D. Davies, P. Molnar, Plate tectonics of the Red Sea and East Africa, Nature 226 (1970) 243–248. https://doi.org/10.1038/226243a0.

[20] J.D. Lowell, G.J. Genik, Sea-floor spreading and structural evolution of the southern Red Sea, AAPG Bull. 56 (1972) 247-259. https://doi.org/10.1306/819a3e56-16c5-11d7-8645000102c1865d.

[21] L. Stieltjes, Evolution tectonique récente du rift d'Asal, Rev. Geogr. Phys. Geol. Dyn. 15 (1973) 425-436.

[22] P. Stoffers, D.A. Ross, Sedimentary history of the Red Sea, Initial Rep. Deep Sea Drill. Proj. 23 (1974) 849-865. https://doi.org/10.2973/dsdp.proc.23.123.1974.

[23] R.C. Searle, D.A. Ross, Geophysical study of the Red Sea axial trough, Geophys. J. R. Astron. Soc. 43 (1975) 555-572. https://doi.org/10.1111/j.1365-246x.1975.tb00647.x.

[24] R.W. Girdler, P. Styles, Two-stage Red Sea floor spreading, Nature 247 (1974) 7-11. https://doi.org/10.1038/247007a0.

[25] H.A. Roeser, Detailed magnetic survey of the southern Red Sea, Geol. Jahrb. 13 (1975) 131-153.

[26] M.E. Gettings, Delineation of the continental margin of the southern Red Sea from new gravity evidence, Saudi Arab. Dir. Gen. Miner. Res. Bull. 2 (1977) K1-K11.

[27] R.W. Girdler, T. Southren, Structure and evolution of the northern Red Sea, Nature 330 (1987) 716-721. https://doi.org/10.1038/330716a0.

[28] X. Le Pichon, J. Francheteau, Plate tectonic analysis of the Red Sea–Gulf of Aden area, Tectonophysics 46 (1978) 369-406. https://doi.org/10.1016/0040-1951(78)90214-7.

[29] R.W. Girdler, C. Brown, D.J.M. Noy, P. Styles, Geophysical survey of the westernmost Gulf of Aden, Philos. Trans. R. Soc. Lond. A 298 (1980) 1-43. https://doi.org/10.1098/rsta.1980.0239.

[30] C. Brown, R.W. Girdler, Structure of the Red Sea at 20º N from gravity data and its implications for continental margins, Nature 298 (1982) 51-53. https://doi.org/10.1038/298051a0.

[31] V. Courtillot, Propagating rifts and continental breakup, Tectonics 1 (1982) 239-250. https://doi.org/10.1029/TC001i003p00239.

[32] W. Bosworth, M. Darwish, P. Crevello, M. Taviani, S. Marshak, Stratigraphic and structural evolution of Zabargad Island (Red Sea, Egypt) since the Early Cretaceous, in: M. El-Ayouty (Ed.), Proc. 3rd Int. Conf. Geol. Arab World, Cairo University, Cairo, 1996, pp. 161-190.

[33] J.R. Cochran, A model for development of Red Sea, AAPG Bull. 67 (1983) 41-69. https://doi.org/10.1306/03B5ACBE-16D1-11D7-8645000102C1865D.

[34] E. Bonatti, P. Colantoni, B. Della Vedova, M. Taviani, Geology of the Red Sea transitional region (22º N-25º N), Oceanol. Acta 7 (1984) 385-398.

[35] R.W. Girdler, Problems concerning the evolution of oceanic lithosphere in the northern Red Sea, Tectonophysics 116 (1985) 109-122. https://doi.org/10.1016/0040-1951(85)90224-0.

[36] S. Joffe, Z. Garfunkel, Plate kinematics of the circum–Red Sea: A re-evaluation, Tectonophysics 141 (1987) 5-23. https://doi.org/10.1016/0040-1951(87)90171-5.

[37] J.L. LaBrecque, N. Zitellini, Continuous seafloor spreading in the Red Sea, AAPG Bull. 69 (1985) 513-524. https://doi.org/10.1306/AD46251F-16F7-11D7-8645000102C1865D.

[38] E. Bonatti, Rifting or drifting in the Red Sea?, Nature 330 (1987) 692-693. https://doi.org/10.1038/330692a0.

[39] A.Y. Izzeldin, Seismic, gravity and magnetic surveys in the central part of the Red Sea, Tectonophysics 143 (1987) 269-306. https://doi.org/10.1016/0040-1951(87)90214-9.

[40] J.M. Gaulier, X. Le Pichon, N. Lyberis, F. Avedik, L. Geli, I. Moretti, A. Deschamps, S. Hafez, Seismic study of the crust of the northern Red Sea and Gulf of Suez, Tectonophysics 153 (1988) 55–88. https://doi.org/10.1016/0040-1951(88)90007-8.

[41] F. Martinez, J.R. Cochran, Structure and tectonics of the northern Red Sea, Tectonophysics 150 (1988) 1-32. https://doi.org/10.1016/0040-1951(88)90293-4.

[42] R.W. Girdler, The case for oceanic crust beneath the Red Sea, Tectonophysics 198 (1991) 275-278. https://doi.org/10.1016/0040-1951(91)90155-L.

[43] P. Guennoc, G. Pautot, M.-F. Le Quentrec, A. Coutelle, Structure of an early oceanic rift in the northern Red Sea, Oceanol. Acta 13 (1990) 145-155.

[44] A.Y. Izzeldin, Transverse structures in the central Red Sea and implications for early oceanic accretion, Geophys. J. 96 (1989) 117-129. https://doi.org/10.1111/j.1365-246X.1989.tb05254.x.

[45] E. Uchupi, D.A. Ross, The geologic enigma of the Red Sea rift, in: V. Ittekkot et al. (Eds.), Facets of Modern Biogeochemistry, Springer, Berlin, 1990, pp. 52–61.

[46] J. Makris, R. Rihm, Shear-controlled evolution of the Red Sea, Tectonophysics 198 (1991) 441-466. https://doi.org/10.1016/0040-1951(91)90166-p.

[47] W. Bosworth, Geological evolution of the Red Sea: Historical background, review, and synthesis, in: N.M.A. Rasul, I.C.F. Stewart (Eds.), The Red Sea, Springer Earth System Sciences, Berlin, 2015, pp. 45-78. https://doi.org/10.1007/978-3-662-45201-1_3.

[48] W. Bosworth, D.F. Stockli, Early magmatism in the greater Red Sea, Can. J. Earth Sci. 53 (2016) 1158-1176. https://doi.org/10.1139/cjes-2016-0019.

[49] W. Bosworth, S.M. Khalil, L. Ligi, D.F. Stockli, K.R. McClay, The northern Red Sea, in: Z. Hamimi et al. (Eds.), The Geology of Egypt, Springer, Cham, 2020, pp. 344-369. https://doi.org/10.1007/978-3-030-15265-9_9.

[50] R. Issachar, J. Ebbing, Y. Dilixiati, New magnetic anomaly map for the Red Sea reveals transtensional structures associated with rotational rifting, Sci. Rep. 12 (2022) 5757. https://doi.org/10.1038/s41598-022-09770-0.

[51] A. Delaunay, G. Baby, J. Fedorik, A.M. Afifi, P. Tapponnier, J. Dyment, Structure and morphology of the Red Sea, from the mid-ocean ridge to the ocean-continent boundary, Tectonophysics 849 (2023) 229728. https://doi.org/10.1016/j.tecto.2023.229728.

[52] T.B. Phillips, J.B. Naliboff, K.J.W. McCaffrey, S. Pan, J. van Hunen, M. Froemchen, The influence of crustal strength on rift geometry and development: insights from 3D numerical modelling, Solid Earth 14 (2023) 369–388. https://doi.org/10.5194/se-14-369-2023.

[53] R. Issachar, P. Haas, N. Augustin, J. Ebbing, Rift and plume: a discussion on active and passive rifting mechanisms in the Afro-Arabian rift based on synthesis of geophysical data, Solid Earth 15 (2024) 807-826. https://doi.org/10.5194/se-15-807-2024.

[54] T. Pensa, A.D. Huertas, A.M. Afifi, Desiccation of the Red Sea basin at the start of the Messinian salinity crisis was followed by major erosion and reflooding from the Indian Ocean, Commun. Earth Environ. 6 (2025) 649. https://doi.org/10.1038/s43247-025-02642-1.

[55] N. Augustin, F.M. van der Zwan, C.W. Devey, B. Brandsdóttir, 13 million years of seafloor spreading throughout the Red Sea Basin, Nat. Commun. 12 (2021) 2427. https://doi.org/10.1038/s41467-021-22586-2.

[56] M. ElGabry, M. Abdelazim, Seismicity of the Red Sea and Gulf of Aden, in: Z. Hamimi et al. (Eds.), Seismotectonics of the East Mediterranean-Red Sea region, Springer, 2025, pp. 235-256. https://doi.org/10.1007/978-3-031-80928-6_14.

[57] G.W. Hughes, R.S. Johnson, Lithostratigraphy of the Red Sea region, GeoArabia 10 (2005) 49-126. https://doi.org/10.2113/geoarabia100349.

[58] Environmental Systems Research Institute (ESRI), ArcGIS Pro, Version 3.2 [software], ESRI, Redlands, CA, USA, 2023. https://www.esri.com/en-us/arcgis/products/arcgis-pro/overview.

[59] H. Fritz, M. Abdelsalam, K.A. Ali, B. Bingen, A.S. Collins, A.R. Fowler, W. Ghebreab, C.A. Hauzenberger, P.R. Johnson, T.M. Kusky, P. Macey, S. Muhongo, R.J. Stern, G. Viola, Orogen styles in the East African Orogen: A review of the Neoproterozoic to Cambrian tectonic evolution, J. Afr. Earth Sci. 86 (2013) 65-106. https://doi.org/10.1016/j.jafrearsci.2013.06.004.

[60] J.D. Walker, J.W. Geissman (Compilers), Geologic Time Scale v. 6.0, Geol. Soc. Am. (2022). https://doi.org/10.1130/2022.CTS006C.

[61] O.I. Okwokwo, N.C. Mitchell, W. Shi, I.C.F. Stewart, A.Y. Izzeldin, How have thick evaporites affected early sea-floor spreading magnetic anomalies in the central Red Sea?, Geophys. J. Int. 229 (2022) 1550-1566. https://doi.org/10.1093/gji/ggac012.

[62] M. Ligi, E. Bonatti, F. Caratori Tontini, A. Cipriani, L. Cocchi, A. Schettino, G. Bortoluzzi, V. Ferrante, S. Khalil, N.C. Mitchell, N. Rasul, Initial burst of oceanic crust accretion in the Red Sea due to edge-driven mantle convection, Geology 39 (2011) 1019-1022. https://doi.org/10.1130/G32243.1.

[63] M. Ligi, E. Bonatti, W. Bosworth, Y. Cai, A. Cipriani, C. Palmiotto, S. Ronca, M. Seyler, Birth of an ocean in the Red Sea: Oceanic-type basaltic melt intrusions precede continental rupture, Gondwana Res. 54 (2018) 150-160. https://doi.org/10.1016/j.gr.2017.11.002.

[64] N.C. Mitchell, Y. Park, Nature of crust in the central Red Sea, Tectonophysics 628 (2014) 123-139. https://doi.org/10.1016/j.tecto.2014.04.029.

[65] A. Schettino, C. Macchiavelli, P.P. Pierantoni, D. Zanoni, N. Rasul, Recent kinematics of the tectonic plates surrounding the Red Sea and Gulf of Aden, Geophys. J. Int. 207 (2016) 457-480. https://doi.org/10.1093/gji/ggw280.

[66] R. Viltres, S. Jónsson, A.O. Alothman, S. Liu, S. Leroy, F. Masson, C. Doubre, R. Reilinger, Present-day motion of the Arabian plate, Tectonics 41 (2022) e2021TC007013. https://doi.org/10.1029/2021TC007013.

[67] R. Issachar, N. Wetzler, S. Engelberg, M. Abelson, Full-length oceanic spreading in the Red Sea: Insights from the spatio-temporal distribution of earthquakes, Geology (2026). https://doi.org/10.1130/G54723.1.

[68] N.C. Mitchell, W. Shi, A.Y. Izzeldin, I.C.F. Stewart, Reconstructing the level of the central Red Sea evaporites at the end of the Miocene, Basin Res. 33 (2021) 1266-1292. https://doi.org/10.1111/bre.12513.

[69] A. ArRajehi, S. McClusky, R. Reilinger, M. Daoud, A. Alchalbi, S. Ergintav, F. Gomez, J. Sholan, F. Bou-Rabee, G. Ogubazghi, B. Haileab, M. Fisseha, L. Asfaw, S. Mahmoud, A. Rayan, R. Bendick, L. Kogan, Geodetic constraints on present-day motion of the Arabian Plate: Implications for Red Sea and Gulf of Aden rifting, Tectonics 29 (2010) TC3011. https://doi.org/10.1029/2009TC002482.

[70] D. Chu, R.G. Gordon, Current plate motions across the Red Sea, Geophys. J. Int. 135 (1998) 313-328. https://doi.org/10.1046/j.1365-246X.1998.00658.x.

[71] G. Pietrantonio, R. Devoti, S. Mahmoud, F. Riguzzi, Kinematics of the Suez-Sinai area from combined GPS velocity field, J. Geodyn. 102 (2016) 231-238. https://doi.org/10.1016/j.jog.2016.10.003.

[72] N.C. Mitchell, M. Ligi, V. Ferrante, E. Bonatti, E. Rutter, Submarine salt flows in the central Red Sea, Geol. Soc. Am. Bull. 122 (2010) 701-713. https://doi.org/10.1130/B26518.1.

[73] P. Feldens, N.C. Mitchell, Salt flows in the central Red Sea, in: N.M.A. Rasul, I.C.F. Stewart (Eds.), The Red Sea: The Formation, Morphology, Oceanography and Environment of a Young Ocean Basin, Springer, Berlin, 2015, pp. 205-218. https://doi.org/10.1007/978-3-662-45201-1_12.

[74] A.Y. Izzeldin, N.C. Mitchell, Shield suture zones control positions of oceanic spreading segment discontinuities in the central Red Sea, in: N.M.A. Rasul, I.C.F. Stewart (Eds.), Rifting and

Sediments in the Red Sea and Arabian Gulf Regions, CRC Press, Boca Raton, 2024, pp. 61-74. https://doi.org/10.1201/9781003321415-5.

[75] A. Sanfilippo, M. Ligi, R. Avanzinelli, V. Basch, A. Bragagni, A. Decarlis, H. Guillou, S. Nomade, N. Rasul, L. Vigliotti, S. Conticelli, Magmatic underplating and crustal intrusions accommodate extension during Red Sea continental rifting, Nat. Commun. 16 (2025) 6488. https://doi.org/10.1038/s41467-025-61598-0.

[76] K.M. Haase, R. Mühe, P. Stoffers, Magmatism during extension of the lithosphere: geochemical constraints from lavas of the Shaban Deep, northern Red Sea, Chem. Geol. 166 (2000) 225-239. https://doi.org/10.1016/S0009-2541(99)00221-1.

[77] F.M. van der Zwan, C.W. Devey, N. Augustin, R.A. Almeev, R.M. Bantan, A. Basaham, Hydrothermal activity at the ultraslow- to slow-spreading Red Sea Rift traced by chlorine in basalt, Chem. Geol. 405 (2015) 63-81. https://doi.org/10.1016/j.chemgeo.2015.04.001.

[78] F.J. Vine, Spreading of the ocean floor: new evidence, Science 154 (1966) 1405-1415. https://doi.org/10.1126/science.154.3755.1405.

Figure Captions

Figure 1. Regional geophysical and surface geological frameworks of the Red Sea basin. (a) Regional free-air gravity anomaly map derived from global potential field grids. (b) Total magnetic intensity anomaly map illustrating regional magnetic fabric anomalies. (c) Regional bathymetric map; red circles denote the major axial deeps and hydrothermal brine pools, and black dots mark Zabargad and Brothers Islands. (d) Bathymetric tracking map highlighting bathymetric profile lines across the primary axial trough (cyan filled profiles) relative to published magnetic, gravity, and seismic transect lines (blue lines). (e) Synthesized surface geological base map outlining Precambrian basement suture trends (red lines), including the Sol Hamed and Nakasib sutures, and distinct crustal age domains/growth phases within the Arabian-Nubian Shield [59]. Data compilation: Potential field and bathymetric grids integrated from the World Digital Magnetic Anomaly Map (WDMAM v2.1), the NOAA National Centers for Environmental Information (NCEI), and the UCSD Topographic/Bathymetric database; base maps generated using Earthstar Geographics imagery.

Figure 2. Reconstructed crustal velocity architecture from regional seismic refraction lines. (a) Crustal velocity columns for the fifteen 1958 VEMA-Atlantis seismic refraction stations (Nos. 170-184), arranged by distance along the Red Sea axis over approximately 1,900 km and compiled from legacy refraction data [13,33]. The columns differentiate two fundamental crustal velocity domains: shield-type continental basement (5.5-6.4 km/s) and oceanic or basic intrusive basement (6.7-7.3 km/s); water depth, basement-refractor depth, and physiographic setting are shown for each station, and the northern, central, and southern provinces are indicated. Displayed with a vertical exaggeration of approximately 43:1. (b) The same section at true scale (V.E. = 1:1) for reference.

Figure 3. Structural inheritance, transform systems, and magnetic fabric variations of the Red Sea. Maps (a-d) isolate the four primary structural trends influencing basin geometry: (a) longitudinal N-S basement faults; (b) inherited Precambrian suture zone trajectories; (c) NW-SE oblique (“Najd”-attributed) trends; and (d) Aqaba-Dead Sea transform-related fault systems. (e) Free-air gravity anomaly map over the southern Red Sea axial ridge, showing a high-amplitude anomaly zone (approximately 110 km wide) that terminates abruptly against the Nakasib Suture Zone, marking a profound crustal-scale boundary. (f) Detailed magnetic map highlighting five distinct groupings of linear magnetic anomalies mapped across the central and southern provinces; these linear, elongated anomalies (delineated by white dashed lines) are interpreted as organized Vine-Matthews seafloor spreading anomalies. Displacements across these magnetic stripes line up with interpreted strike-slip faults derived from transform trends, demonstrating that inherited Precambrian structures and younger transform systems actively control the segmentation and lateral offset of the newly formed oceanic domain.

Figure 4. Potential-field enhancement products used for structural interpretation (Section 2.1). Top row, free-air gravity: (a) upward continuation to 5 km, (b) downward continuation to 2 km, (c) first vertical derivative, (d) tilt derivative. Bottom row, total magnetic intensity: (e) upward continuation to 5 km, (f) downward continuation to 2 km, (g) first vertical derivative, (h) analytic signal. All panels share the same extent and projection, served as operational lineament-tracing criterion and interpretation tools.

Figure 5. Data-index map of all digitized and compiled datasets. Onshore suture traces digitized from the geological synthesis (Fig. 1e; red) with their offshore projections (black dashed); exploration wells Jiddah-1, Maghersum-1, and Durwara-2 (red circles); Vine (1966) model profiles at 16° and 20° N [78] (black); the multichannel seismic reflection survey area and the Izzeldin 2D profile (Fig. 9); the Brown and Girdler and Tramontini and Davies 2D profiles (Fig. 9); the 1958 VEMA-Atlantis refraction stations Nos. 170-184 (Fig. 2; yellow); and the six shore-to-shore group profiles (Group 1 AA/BB and Groups 2-5) used in Figs. 6-8 and 10.

Figure 6. Profile A-A′ and orientation statistics. (a) total-field magnetic anomaly along profile A-A′ (259.6 km, N61.0°E; endpoint coordinates annotated), with the best-fit magnetic symmetry axis (115 km, $r = 0.68$) and the geodetic midpoint (129.8 km). (b) Rose diagram of the four structural trends (28 lineaments; mean axial azimuths and cumulative lengths from the supplementary workbook). (c) Rose diagram of the five magnetic stripe groups (13 segments; per-group mean azimuths and mean lengths).

Figure 7. Shore-to-shore profiles for stripe Groups 1-5, showing bathymetry (blue), total magnetic intensity (black), and free-air gravity (red) along each representative profile. Panel headers give profile length, the mirror-symmetry correlation r of the magnetic profile about its best-fit axis (Section 2.4), midpoint coordinates, and the axial-window width (bathymetric half-depth method; shaded); the axial windows are used for the amplitude statistics of Fig. 10.

Figure 8. Two-dimensional forward magnetic models along profiles A-A′ (top) and B-B′ (bottom). Observed anomalies (dots), calculated response (green), and residual (red); model fits are $R^2 = 0.86$ (RMS 41.8 nT) for A-A′ and $R^2 = 0.88$ (RMS 32.1 nT) for B-B′. Each model comprises mirror-symmetric, vertically bounded polarity blocks (susceptibility 0.002 cgs) within a 3-km-thick magnetized basement layer beneath a non-magnetic sedimentary section including the Miocene evaporites; the modelled spreading axes lie at 124 km (A-A′) and 108 km (B-B′), and mirror-symmetry statistics are annotated.

Figure 9. Geophysical benchmarks and two-dimensional crustal forward models of the Central Red Sea. All transects are recompiled from primary literature to provide independent geometric and density constraints on the subsurface architecture [14,39,40]. (a) Regional free-air gravity transect and matching 2D forward model, illustrating that fitting the observed axial gravity anomaly requires a high-density crustal core (3.0 g/cm^3). (b) Regional Bouguer gravity anomaly and lithospheric density model, where the prominent +100 mGal anomaly corresponds to displacement of standard continental basement (2.67 g/cm^3) by high-density mafic crust and anomalous underlapping lithospheric mantle (3.25 g/cm^3). (c) Two-dimensional gravity model across the western margin, capturing the structural transition from the un-extended continental shield into dense oceanic-type basement beneath the Main Trough. (d) Composite multichannel seismic reflection interpretation compiled across seven regional profiles, where continuous, high-amplitude reflections demonstrate a persistent oceanic crustal domain extending up to 80 km laterally beyond the active axial trough. Profile locations are shown in Fig. 5.

Figure 10. Amplitude statistics and alignment tests for the five stripe groups. (a-c) Distributions of magnetic anomaly, free-air gravity, and bathymetric roughness within each group's axial window (diamonds: means). (d-e) Gravity-high width and magnetic-anomaly width versus latitude. (f) Exact permutation test of the {Group 3, Group 4} versus {Group 1, Group 2, Group 5} split over all $C(5,2) = 10$ possible splits: no statistic is significant (minimum attainable $p = 0.10$; observed

minimum p = 0.20). (g) Chance-alignment null test (Sections 2.6, 4.4): the Nakasib suture trace meets the Atlantis II Transform Fault within 0.30 km (observation-specific chance-alignment $p \approx 0.001$ against the 15-25°N search space; generic ±25 km corridor prior $p = 0.045$), whereas the Sol Hamed suture lies 105 km from the northern limit of coherent lineations (outside the corridor). Per-group statistics are listed in the supplementary workbook.

Figure 11. Euler small-circle test of the four structural trends and the Aqaba-Dead Sea set. (a) The 28 mapped lineaments in their trend colours, each with the small-circle azimuth predicted at its midpoint by the Nubia-Arabia pole of [69] (dashed vanes). (b) The nine Aqaba-Dead Sea lineaments with predictions from both the Nubia-Arabia pole [69] (grey) and an Arabia-Sinai pole derived by differencing the Arabia and Sinai angular velocities of [71] (green). (c) Mean angular offsets (±1 s.d.): N-S basement 39.5°, suture-related 9.9°, "Najd"-attributed 75.4°, Aqaba-Dead Sea 22.4°. (d) Per-lineament comparison for the Aqaba-Dead Sea set: the Arabia-Sinai pole improves the fit on all nine lineaments (mean 22.4° to 5.1°). Frames rotated 29° so the basin axis is vertical. Base map: Esri, Maxar, Earthstar Geographics.

Figure 12. Bathymetric data-source comparison over the Atlantis II corridor, with the stripe-offset construction. (a) The UCSD grid (operative base, Section 2.5); (b) GMRT v4.5 compiled (blended, 0% NoData); (c) GMRT v4.5 masked (verified multibeam only; 90% NoData in this corridor). All panels share the same extent and colour scale. Overlaid on each: the mapped Atlantis II Transform Fault trace (red dashed), the Group 1 (Stripes L10 in the workbook) and Group 2 (Stripes L5 in the workbook) magnetic stripe segments with their trend projections (dotted), the two transform crossings (triangles), and the 49.6 km along-transform offset (black bar; ±4.8 km under ±1.5° azimuth perturbation). Sources: UCSD (topex.ucsd.edu); GMRT v4.5.

Figure 13. Onshore-offshore suture continuity tests. (a) Sol Hamed and (b) Nakasib: onshore suture trace (geology, Fig. 1e; red), its seaward projection (red dashed) with ±10° azimuth corridor (tan), the offshore magnetic suture zone (blue band; widths 91.3 km and 94.6 km) with its bottom boundary as the tested element, and the cross-track offset to the bottom boundary (13.2 km and 10.4 km; zoom insets, 88 × 88 km). Frames rotated 29° so the basin axis is vertical. (c) Chance-alignment null test in the Fig. 10g idiom: observed offsets with sensitivity bars (choice of onshore trend), the ±25 km corridor ($p = 0.045$ against the 15-25°N search space, 1107 km), and per-row probabilities at the observed offsets ($p = 0.024$ and 0.019 for the two suture-boundary alignments; $p = 0.001$, repeated from Fig. 10g/Section 3.2, for the Nakasib-transform crossing). Individual estimates are listed in the supplementary workbook. Base map: Esri, Maxar, Earthstar Geographics.

Figure 14. Integrated domain-based evolutionary model for Red Sea seafloor spreading. (a) Total magnetic intensity with the synthesized Arabian-Nubian Shield terranes and sutures (Fig. 1e convention), the axial deeps, and the northern and southern sub-zones of the central Red Sea, and seismic refraction line 180-181, which records deep crustal velocities of 6.97 km/s. (b) Central Red Sea detail: the Sol Hamed and Nakasib suture plateaus (black dashed) bounding the interpreted older oceanic domain, the exploration wells Jiddah-1, Maghersum-1, and Durwara-2, and seismic refraction line 180-181, which records deep crustal velocities of 6.97 km/s on the eastern portion of profile A-A′. (c) Bathymetric synthesis of the final domain configuration: the northern Continental Rift, the central domain bounded by the Sol Hamed and Nakasib suture plateaus, and the southern Active Sea Floor Spreading domain. Colour bars: magnetic anomaly (a, b) and bathymetry (c).

Figure 15. Alternative (non-spreading) forward models of profile A-A′, constructed with the same basement-top geometry, 3-km magnetized layer, and geomagnetic field parameters as the Fig. 8 spreading model. (a) Fully continental models: a uniform basement with induced magnetization only fits not at all, even at its best-fit susceptibility ($R^2 = 0.01$; blue dashed); step-faulted blocks (10-20 km wide) with unorganized (randomly assigned) polarities, the typical case shown fits at $R^2 = 0.09$, and the best of 3,000 random-polarity trials reaches only $R^2 = 0.83$ ($P(R^2 \geq 0.86) < 0.0003$); a freely tuned magnetization can equal the spreading model's fit, but only by reproducing the alternating, reversal-organized pattern that spreading predicts. (b) The same continental background as (a) (susceptibility held fixed) plus eight discrete mafic intrusions at optimized positions: $R^2 = 0.70$ (RMS 61.3 nT); the intrusions cluster near the axis and the flanking alternation is not reproduced. (c) Fit summary: R^2 rises systematically with the degree of oceanic-type, reversal-organized magnetization, from 0.01 (continental, induced only) to 0.86 (reversal-organized accretion, Fig. 8). Block colour: magnetization (normalized). Model construction and fit statistics are listed in the supplementary workbook.

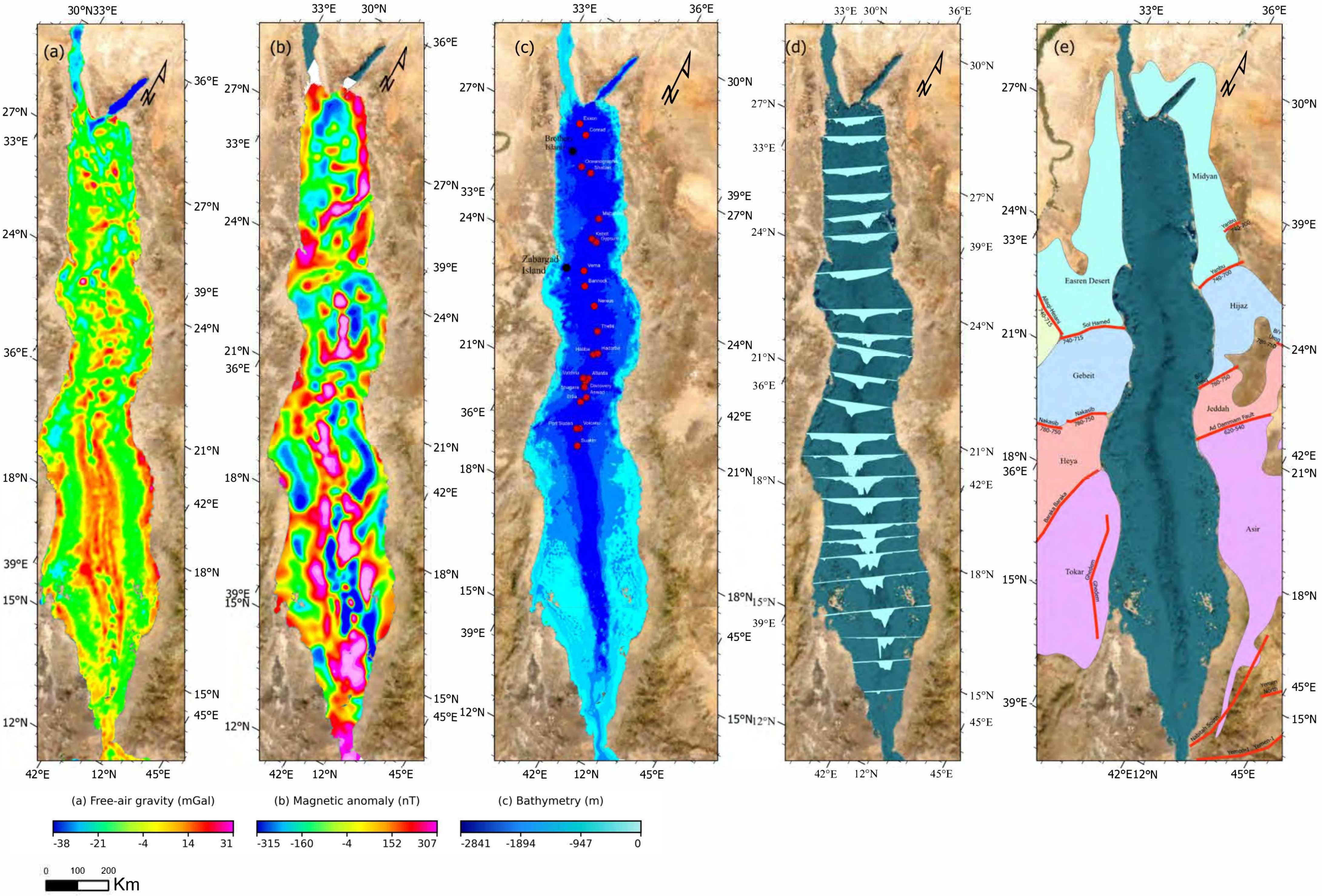

(a)
(b)
(c)
(d)
(e)
Brothers Island
Zabargad Island
Midyan
Easren Desert
Hijaz
Gebeit
Jeddah
Heya
Asir
Tokar
Sol Hamed
Nakasib
Ad Dammam Fault
(a) Free-air gravity (mGal)
-38 -21 -4 14 31
(b) Magnetic anomaly (nT)
-315 -160 -4 152 307
(c) Bathymetry (m)
-2841 -1894 -947 0
0 100 200
Km

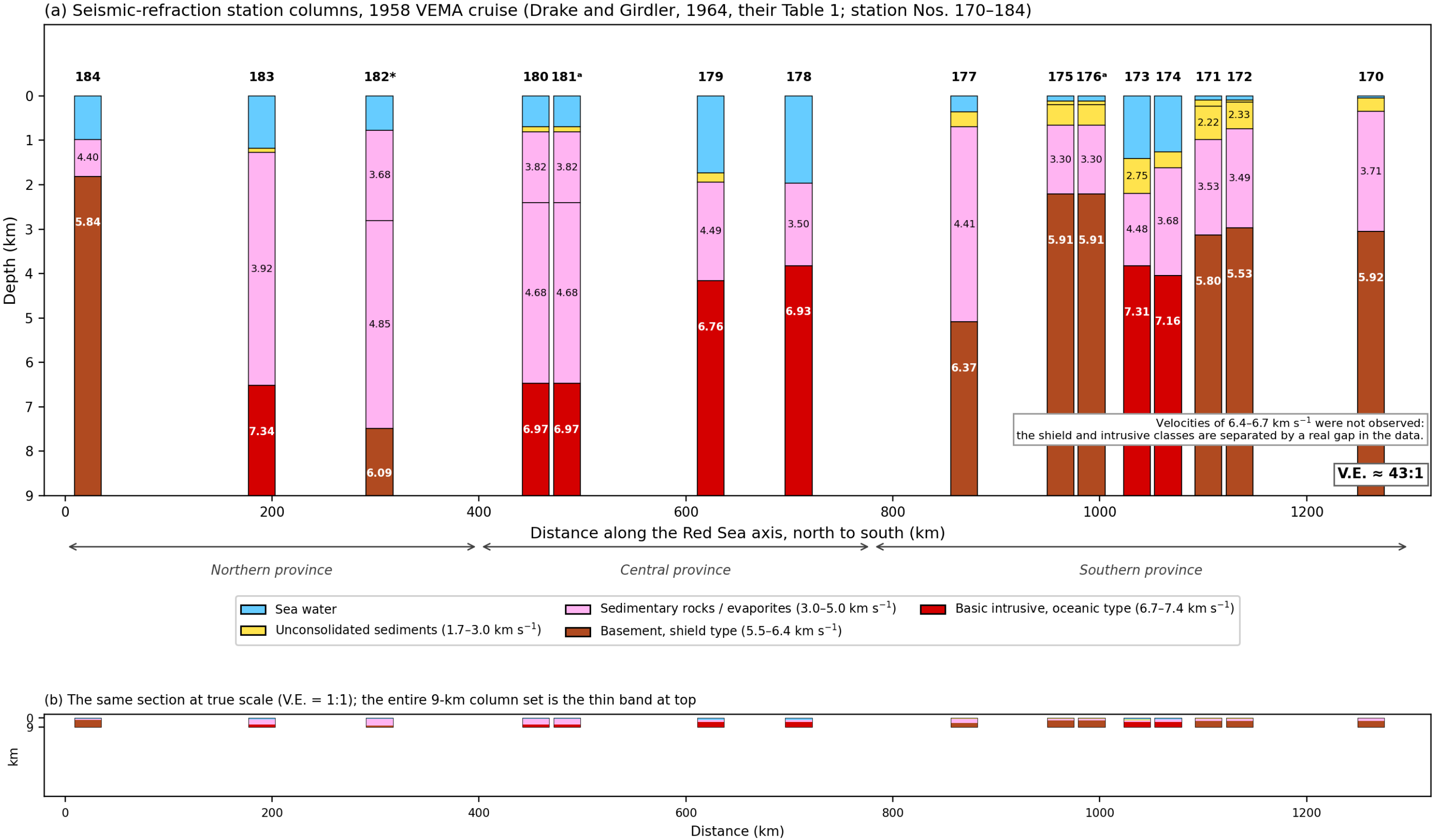
(a) Seismic-refraction station columns, 1958 VEMA cruise (Drake and Girdler, 1964, their Table 1; station Nos. 170–184)
184
183
182*
180
181ᵃ
179
178
177
175
176ᵃ
173
174
171
172
170
4.40
5.84
3.92
7.34
3.68
4.85
6.09
3.82
4.68
6.97
4.49
6.76
3.50
6.93
4.41
6.37
3.30
5.91
2.75
4.48
7.31
3.68
7.16
2.22
3.53
5.80
2.33
3.49
5.53
3.71
5.92
Depth (km)
Distance along the Red Sea axis, north to south (km)
Velocities of 6.4–6.7 km s⁻¹ were not observed: the shield and intrusive classes are separated by a real gap in the data.
V.E. ≈ 43:1
Northern province
Central province
Southern province
Sea water
Unconsolidated sediments (1.7–3.0 km s⁻¹)
Sedimentary rocks / evaporites (3.0–5.0 km s⁻¹)
Basement, shield type (5.5–6.4 km s⁻¹)
Basic intrusive, oceanic type (6.7–7.4 km s⁻¹)
(b) The same section at true scale (V.E. = 1:1); the entire 9-km column set is the thin band at top
km
Distance (km)

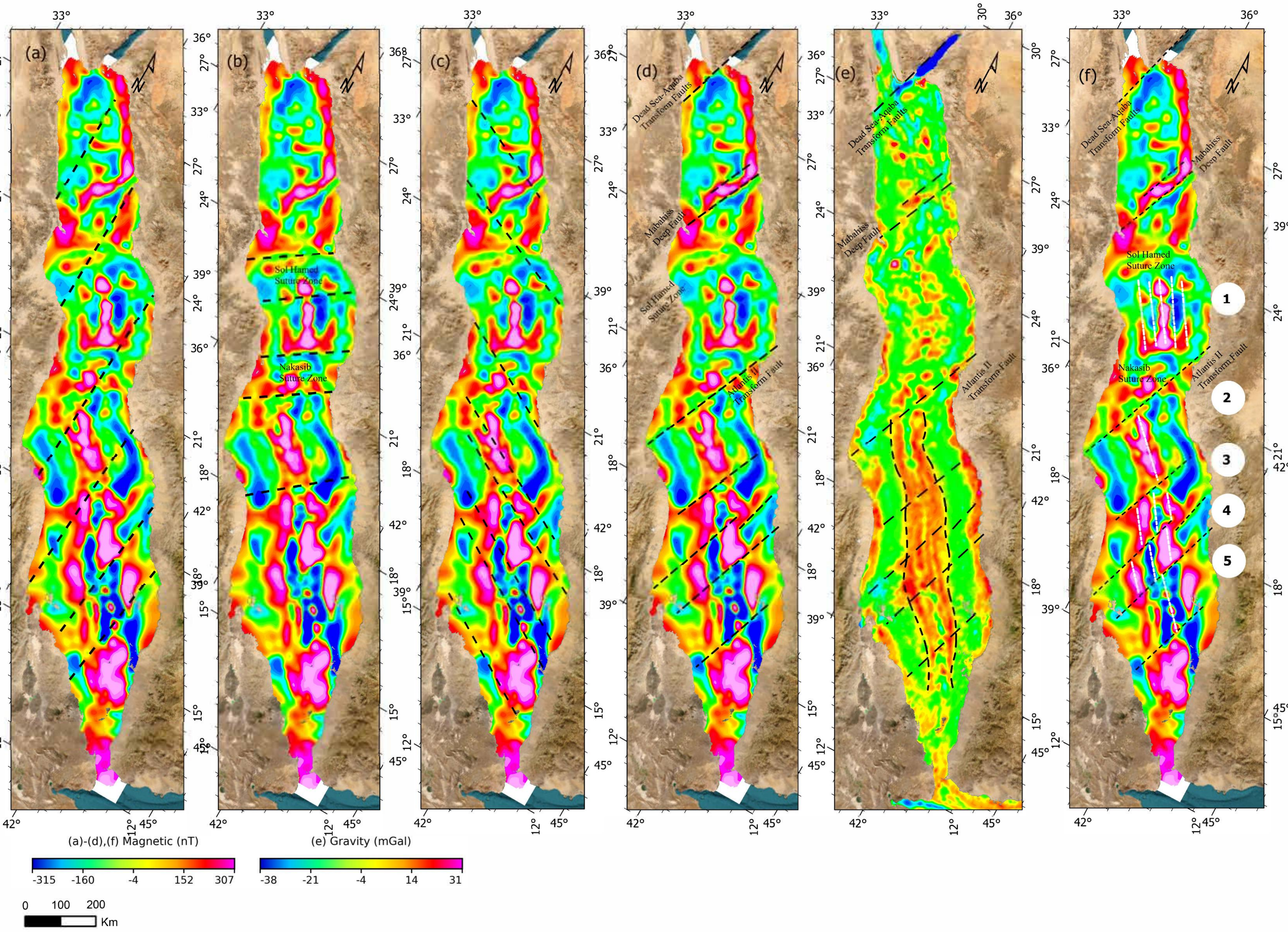
(a)
(b)
(c)
(d)
(e)
(f)
Sol Hamed Suture Zone
Nakasib Suture Zone
Dead Sea-Aqaba Transform Faults
Mabahiss Deep Fault
Atlantis II Transform Fault
1
2
3
4
5
(a)-(d),(f) Magnetic (nT)
(e) Gravity (mGal)
-315
-160
-4
152
307
-38
-21
-4
14
31
0
100
200
Km

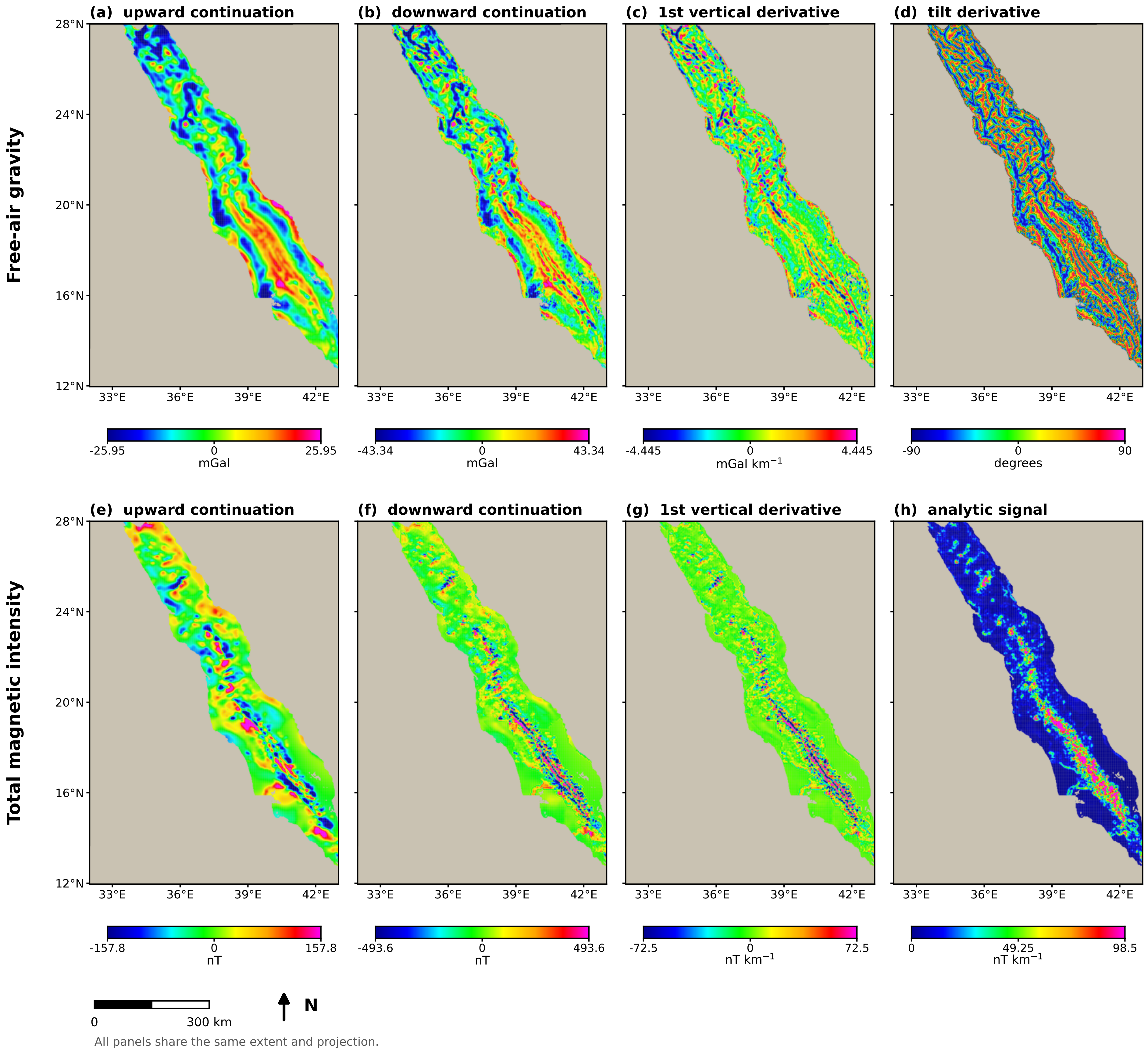

Free-air gravity
(a) upward continuation
(b) downward continuation
(c) 1st vertical derivative
(d) tilt derivative
28°N
24°N
20°N
16°N
12°N
33°E
36°E
39°E
42°E
-25.95
0
25.95
mGal
-43.34
0
43.34
mGal
-4.445
0
4.445
mGal km⁻¹
-90
0
90
degrees
Total magnetic intensity
(e) upward continuation
(f) downward continuation
(g) 1st vertical derivative
(h) analytic signal
-157.8
0
157.8
nT
-493.6
0
493.6
nT
-72.5
0
72.5
nT km⁻¹
0
49.25
98.5
nT km⁻¹
0
300 km
N
All panels share the same extent and projection.

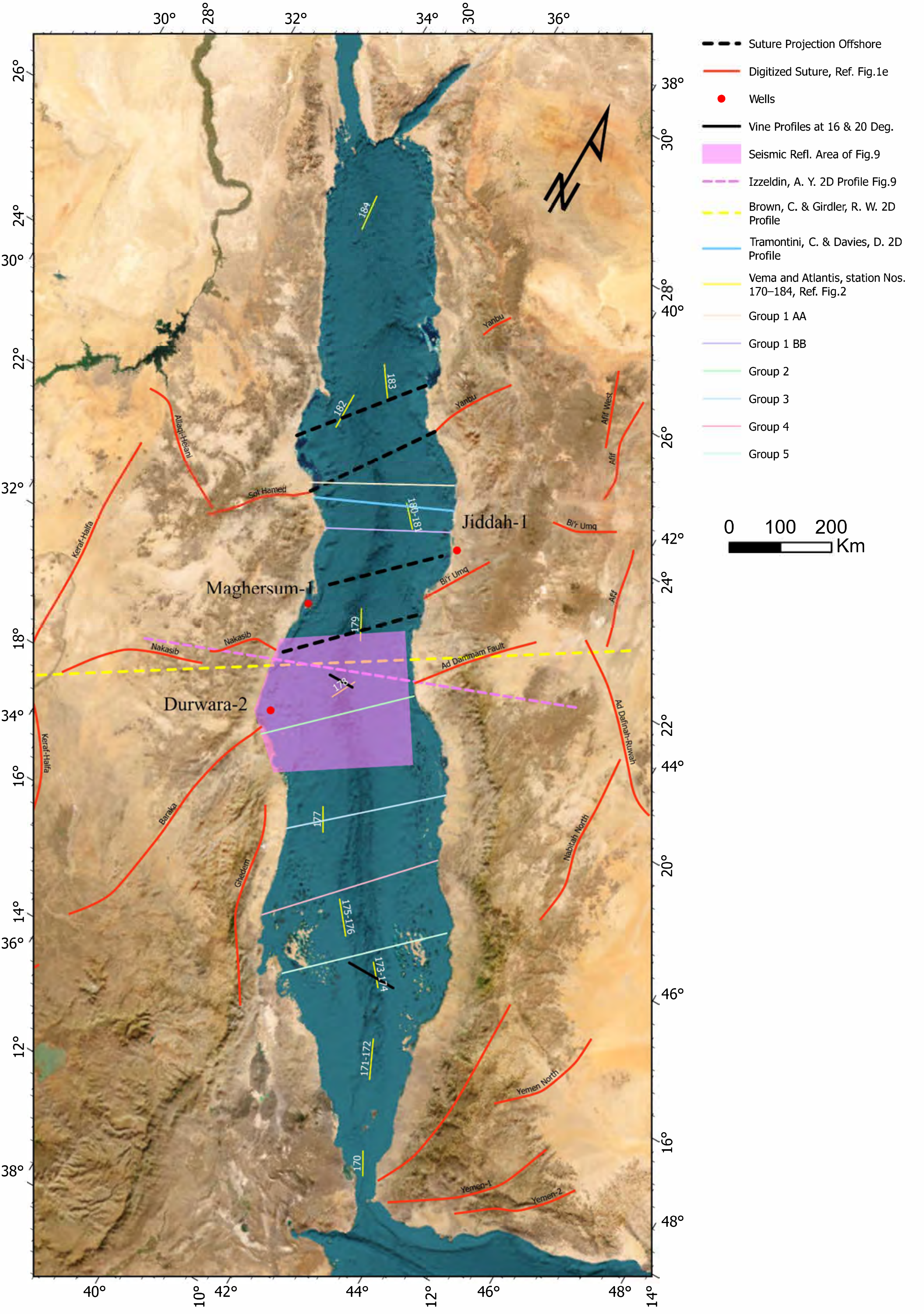

Suture Projection Offshore
Digitized Suture, Ref. Fig.1e
Wells
Vine Profiles at 16 & 20 Deg.
Seismic Refl. Area of Fig.9
Izzeldin, A. Y. 2D Profile Fig.9
Brown, C. & Girdler, R. W. 2D Profile
Tramontini, C. & Davies, D. 2D Profile
Vema and Atlantis, station Nos. 170–184, Ref. Fig.2
Group 1 AA
Group 1 BB
Group 2
Group 3
Group 4
Group 5
0 100 200 Km
Jiddah-1
Maghersum-1
Durwara-2
Allaqi-Heiani
Sol Hamed
Keraf-Haifa
Nakasib
Baraka
Ghedem
Yanbu
Afif West
Afif
Bi'r Umq
Ad Damman Fault
Ad Dafinah-Ruwah
Nabitah North
Yemen North
Yemen-1
Yemen-2
184
183
182
180-181
179
178
177
175-176
173-174
171-172
170

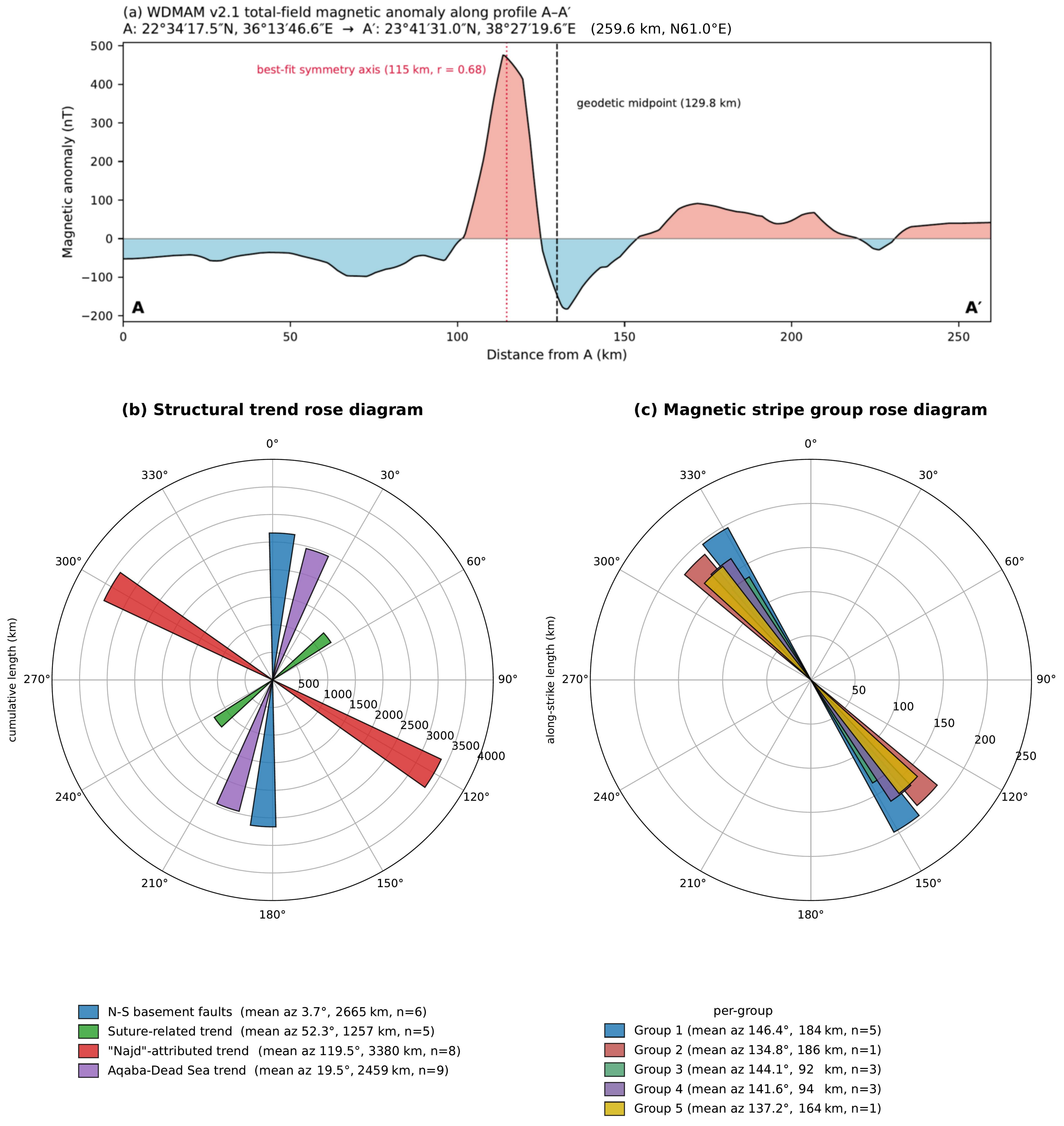
(a) WDMAM v2.1 total-field magnetic anomaly along profile A–A′
A: 22°34′17.5″N, 36°13′46.6″E → A′: 23°41′31.0″N, 38°27′19.6″E (259.6 km, N61.0°E)
best-fit symmetry axis (115 km, r = 0.68)
geodetic midpoint (129.8 km)
Magnetic anomaly (nT)
Distance from A (km)
A
A′
(b) Structural trend rose diagram
cumulative length (km)
(c) Magnetic stripe group rose diagram
along-strike length (km)
N-S basement faults (mean az 3.7°, 2665 km, n=6)
Suture-related trend (mean az 52.3°, 1257 km, n=5)
"Najd"-attributed trend (mean az 119.5°, 3380 km, n=8)
Aqaba-Dead Sea trend (mean az 19.5°, 2459 km, n=9)
per-group
Group 1 (mean az 146.4°, 184 km, n=5)
Group 2 (mean az 134.8°, 186 km, n=1)
Group 3 (mean az 144.1°, 92 km, n=3)
Group 4 (mean az 141.6°, 94 km, n=3)
Group 5 (mean az 137.2°, 164 km, n=1)

■ axial window (bathymetric half-depth method; used for all mag/grav/bathy amplitude statistics in Fig. 10 and the latitude-trend analysis)

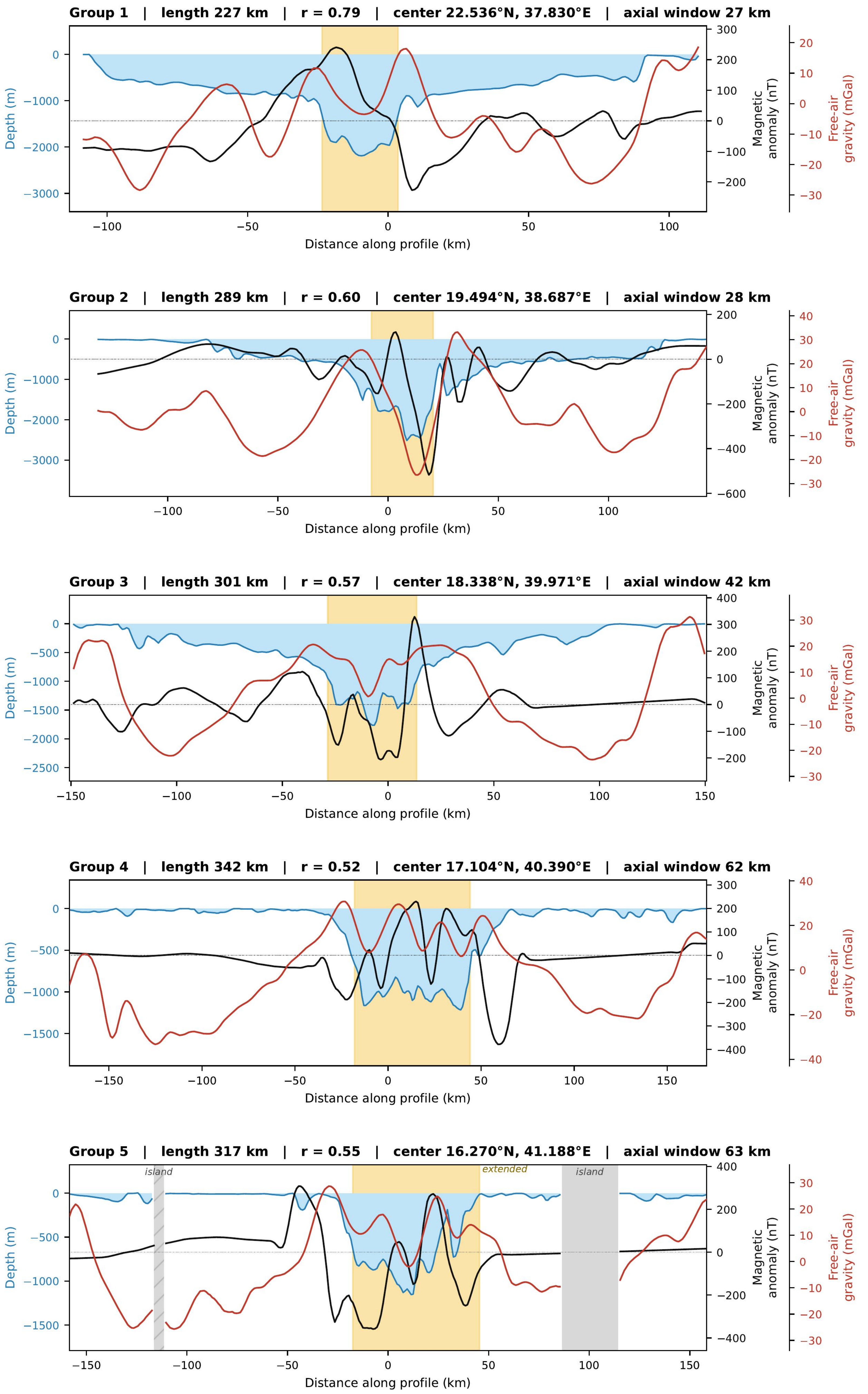

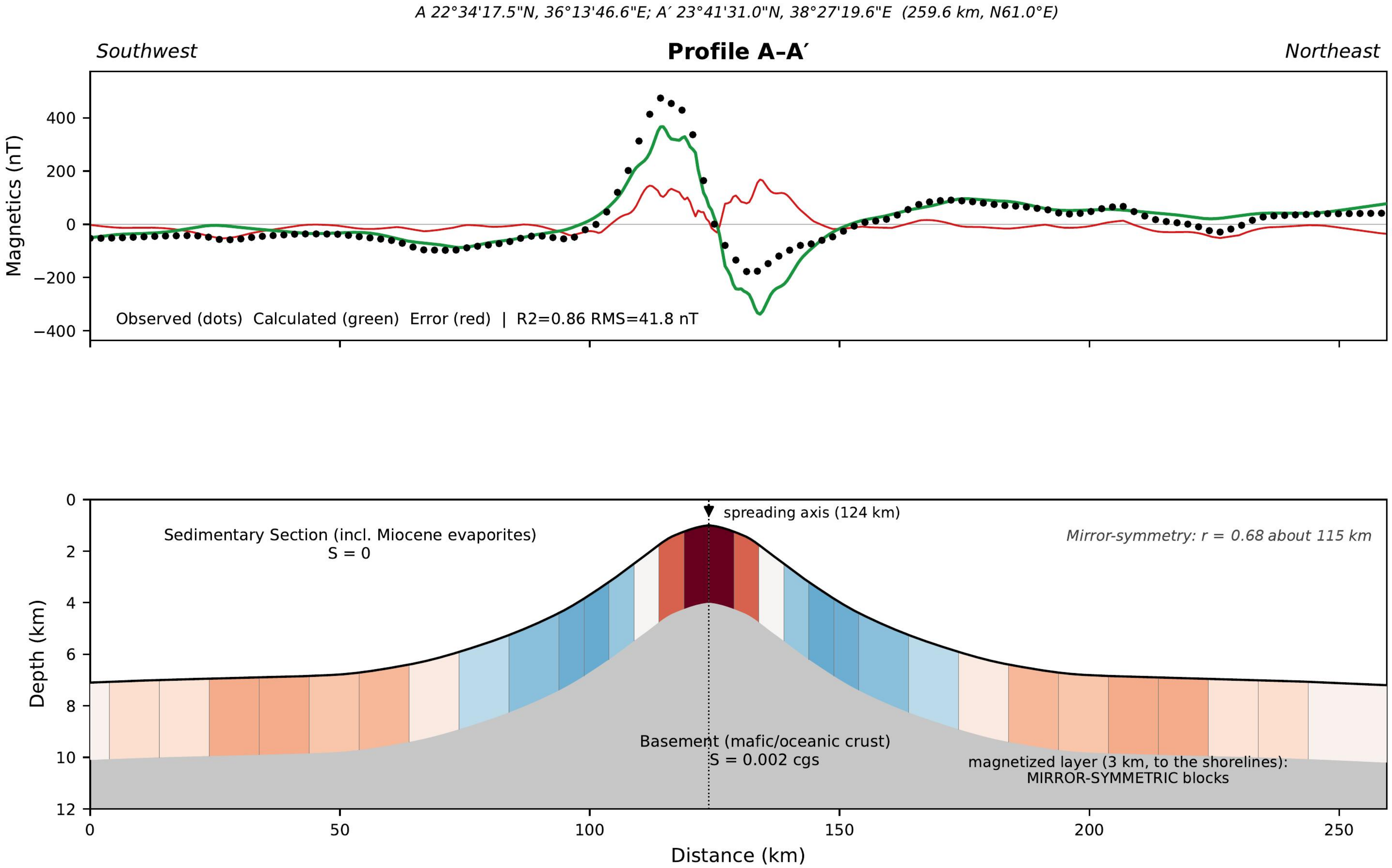
A 22°34'17.5"N, 36°13'46.6"E; A′ 23°41'31.0"N, 38°27'19.6"E (259.6 km, N61.0°E)
Southwest
Profile A–A′
Northeast
Magnetics (nT)
Observed (dots) Calculated (green) Error (red) | R2=0.86 RMS=41.8 nT
spreading axis (124 km)
Sedimentary Section (incl. Miocene evaporites)
S = 0
Mirror-symmetry: r = 0.68 about 115 km
Depth (km)
Basement (mafic/oceanic crust)
S = 0.002 cgs
magnetized layer (3 km, to the shorelines):
MIRROR-SYMMETRIC blocks
Distance (km)

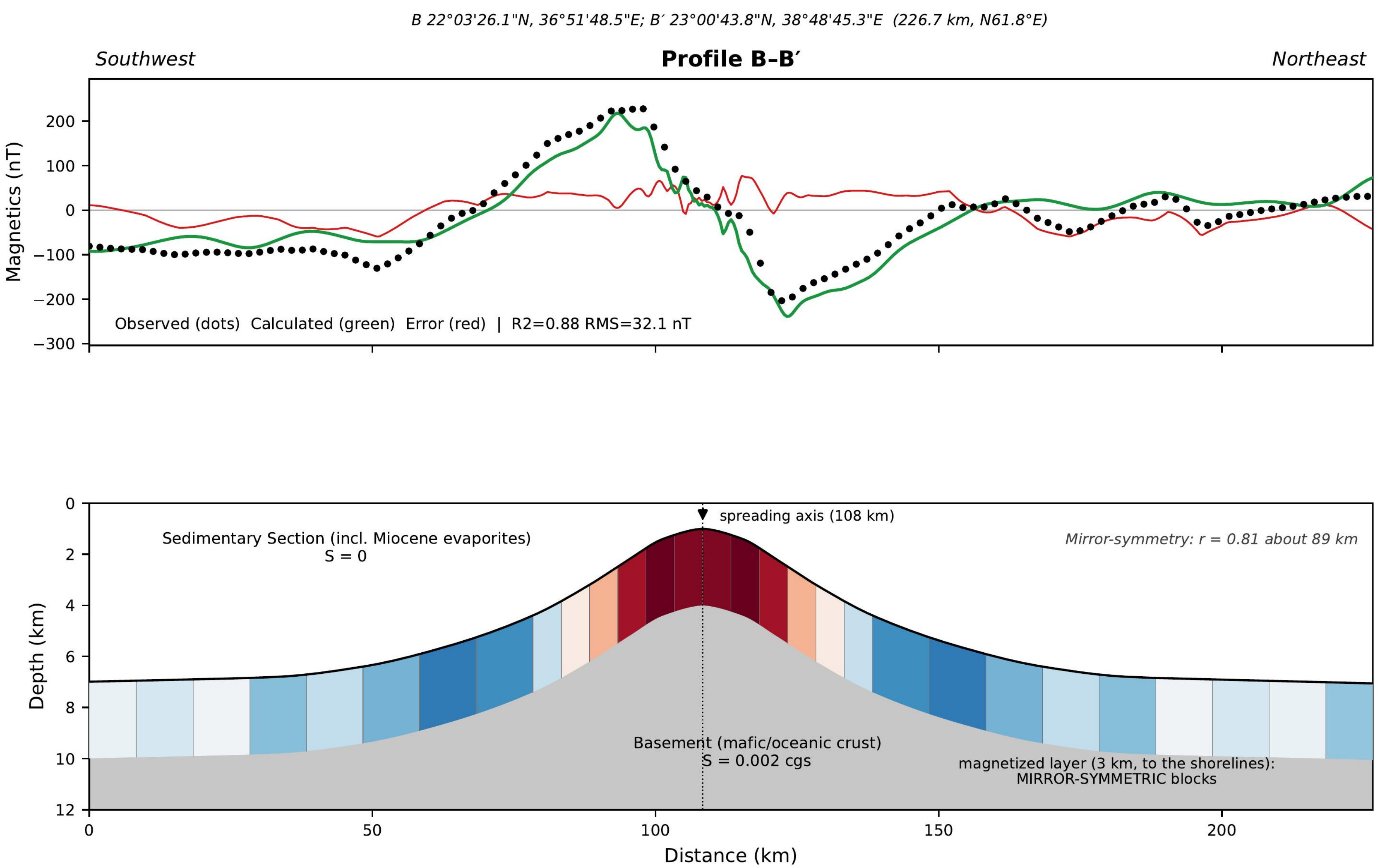
B 22°03'26.1"N, 36°51'48.5"E; B′ 23°00'43.8"N, 38°48'45.3"E (226.7 km, N61.8°E)
Southwest
Profile B–B′
Northeast
Magnetics (nT)
Observed (dots) Calculated (green) Error (red) | R2=0.88 RMS=32.1 nT
spreading axis (108 km)
Sedimentary Section (incl. Miocene evaporites)
S = 0
Mirror-symmetry: r = 0.81 about 89 km
Depth (km)
Basement (mafic/oceanic crust)
S = 0.002 cgs
magnetized layer (3 km, to the shorelines):
MIRROR-SYMMETRIC blocks
Distance (km)

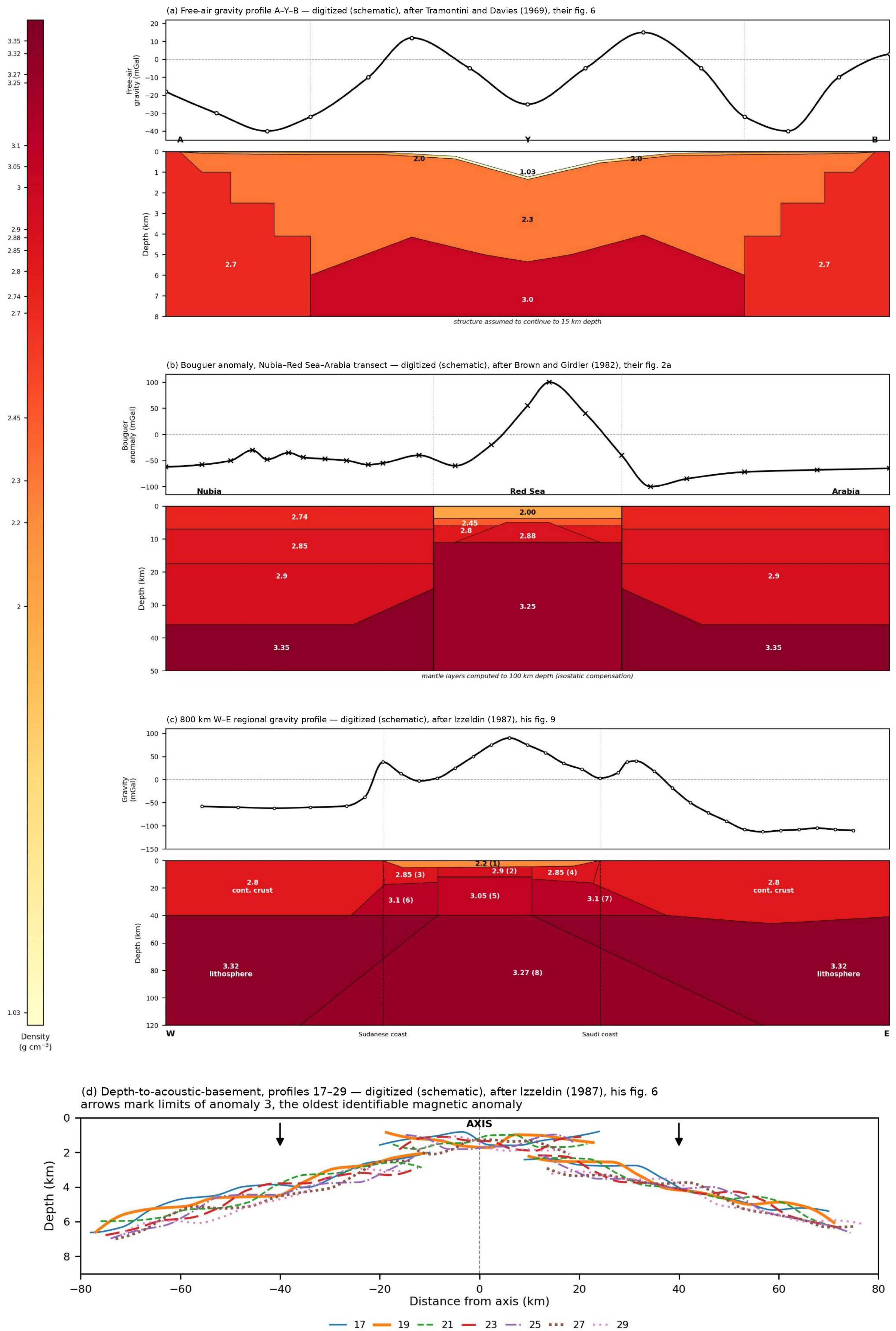
(a) Free-air gravity profile A–Y–B — digitized (schematic), after Tramontini and Davies (1969), their fig. 6
Free-air gravity (mGal)
A
Y
B
Depth (km)
2.0
1.03
2.0
2.3
2.7
3.0
2.7
structure assumed to continue to 15 km depth
(b) Bouguer anomaly, Nubia–Red Sea–Arabia transect — digitized (schematic), after Brown and Girdler (1982), their fig. 2a
Bouguer anomaly (mGal)
Nubia
Red Sea
Arabia
Depth (km)
2.74
2.00
2.45
2.8
2.88
2.85
2.9
3.25
2.9
3.35
3.35
mantle layers computed to 100 km depth (isostatic compensation)
(c) 800 km W–E regional gravity profile — digitized (schematic), after Izzeldin (1987), his fig. 9
Gravity (mGal)
Depth (km)
2.2 (1)
2.85 (3)
2.9 (2)
2.85 (4)
2.8 cont. crust
2.8 cont. crust
3.1 (6)
3.05 (5)
3.1 (7)
3.32 lithosphere
3.27 (8)
3.32 lithosphere
W
Sudanese coast
Saudi coast
E
Density (g cm^{-3})
(d) Depth-to-acoustic-basement, profiles 17–29 — digitized (schematic), after Izzeldin (1987), his fig. 6
arrows mark limits of anomaly 3, the oldest identifiable magnetic anomaly
AXIS
Depth (km)
Distance from axis (km)
17
19
21
23
25
27
29

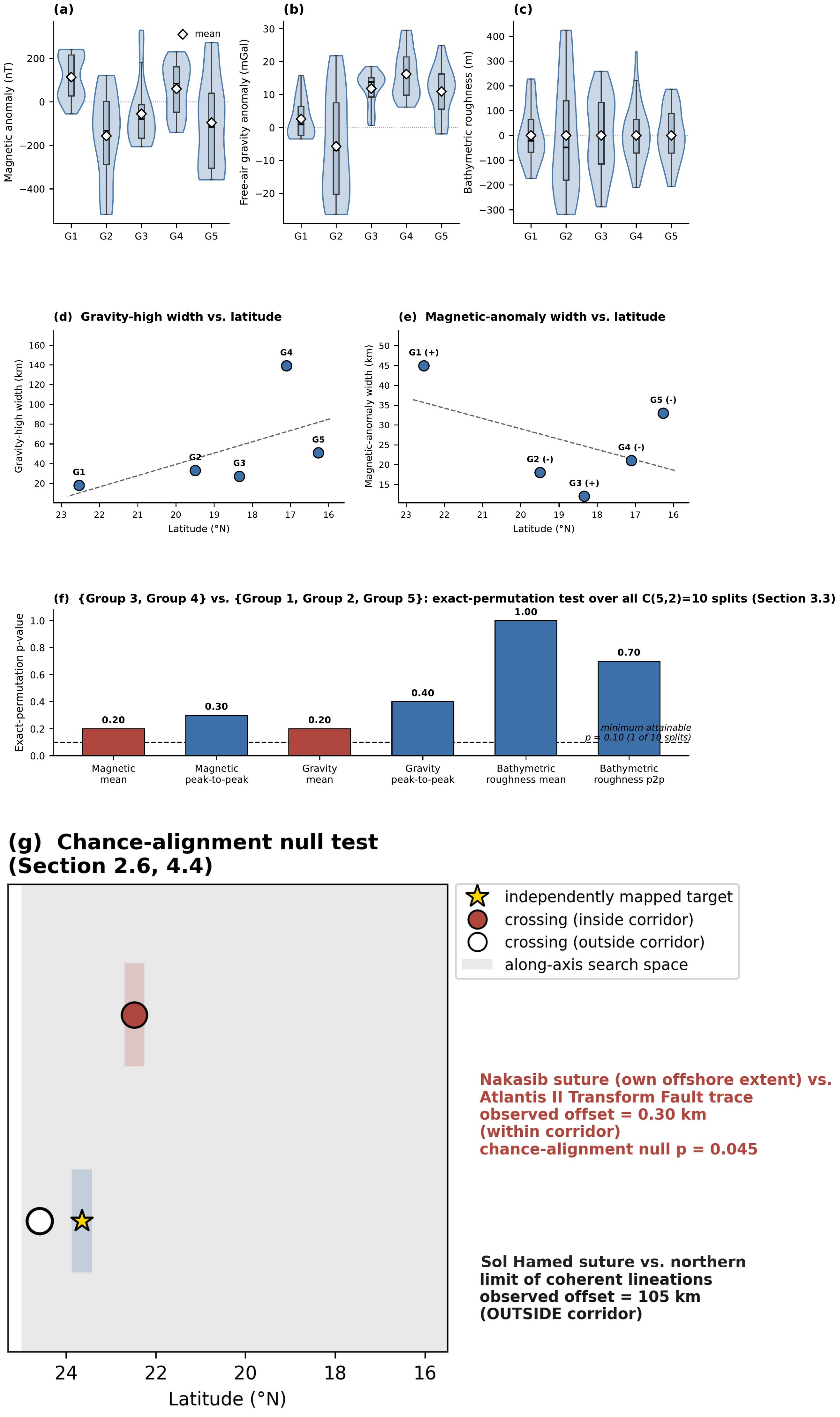
(a)
mean
Magnetic anomaly (nT)
G1 G2 G3 G4 G5
(b)
Free-air gravity anomaly (mGal)
G1 G2 G3 G4 G5
(c)
Bathymetric roughness (m)
G1 G2 G3 G4 G5
(d) Gravity-high width vs. latitude
Gravity-high width (km)
G1
G2
G3
G4
G5
Latitude (°N)
(e) Magnetic-anomaly width vs. latitude
Magnetic-anomaly width (km)
G1 (+)
G2 (-)
G3 (+)
G4 (-)
G5 (-)
Latitude (°N)
(f) {Group 3, Group 4} vs. {Group 1, Group 2, Group 5}: exact-permutation test over all C(5,2)=10 splits (Section 3.3)
Exact-permutation p-value
0.20
0.30
0.20
0.40
1.00
0.70
minimum attainable
p = 0.10 (1 of 10 splits)
Magnetic mean
Magnetic peak-to-peak
Gravity mean
Gravity peak-to-peak
Bathymetric roughness mean
Bathymetric roughness p2p
(g) Chance-alignment null test
(Section 2.6, 4.4)
independently mapped target
crossing (inside corridor)
crossing (outside corridor)
along-axis search space
Nakasib suture (own offshore extent) vs.
Atlantis II Transform Fault trace
observed offset = 0.30 km
(within corridor)
chance-alignment null p = 0.045
Sol Hamed suture vs. northern
limit of coherent lineations
observed offset = 105 km
(OUTSIDE corridor)
24 22 20 18 16
Latitude (°N)

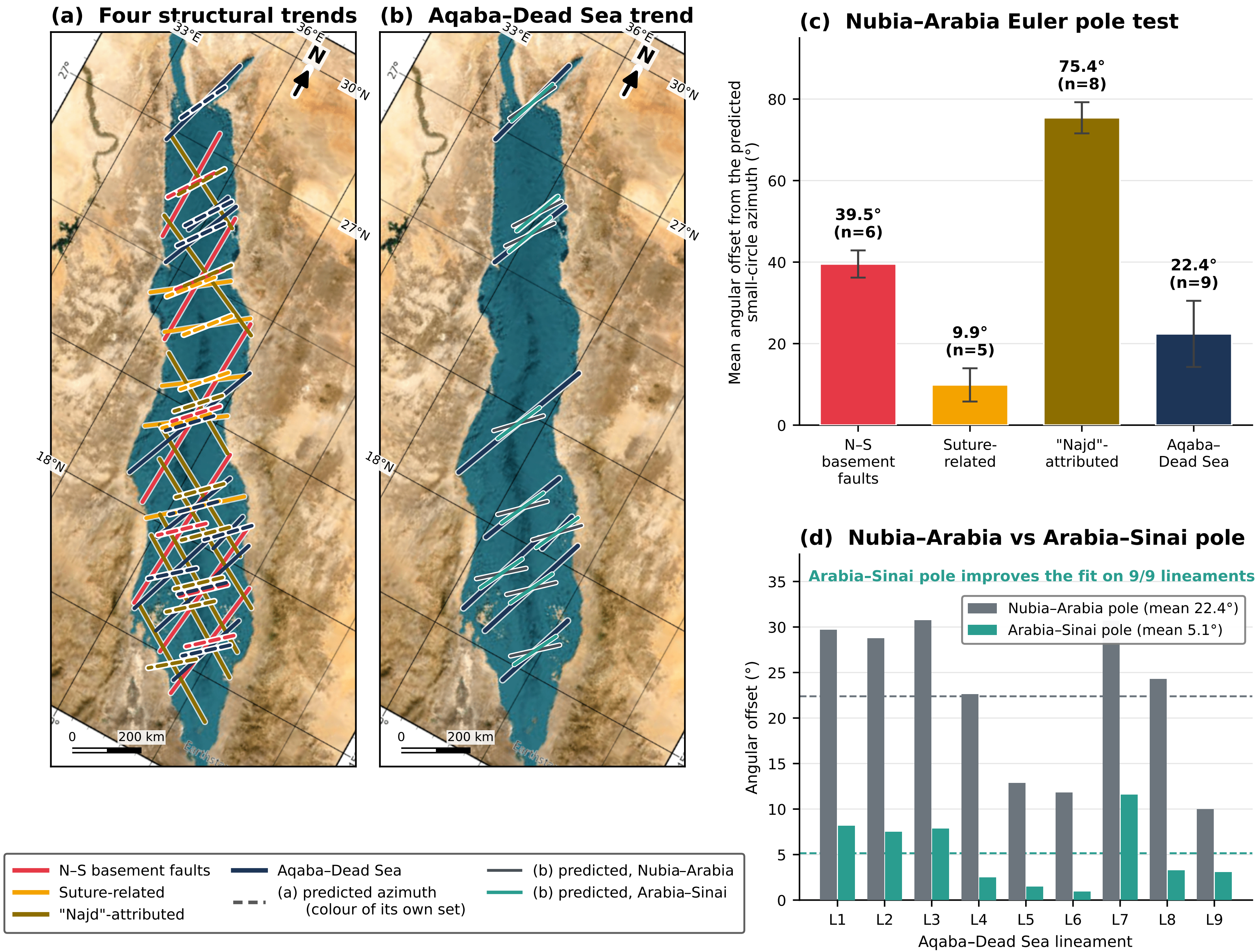

Nubia–Arabia Euler pole: 31.7°N, 24.6°E, 0.369°/Myr (ArRajehi et al., 2010).

Arabia–Sinai Euler pole: 30.78°N, 28.23°W, 0.061°/Myr, derived by differencing the Arabia and Sinai angular velocities of Pietrantonio et al. (2016), their Table 1.

Each mapped lineament (coloured) is drawn with the small-circle azimuth predicted at its midpoint
In (a) the vane is dashed and carries its own set's colour;
in (b) grey and green mark the two poles tested.
The angle between line and vane is the offset plotted in (c) and (d).

Bars in (c) are means ± 1 s.d.

Frames rotated 29° so the basin axis is vertical.
Graticule at 3°.

Base map: Esri, Maxar, Earthstar Geographics.

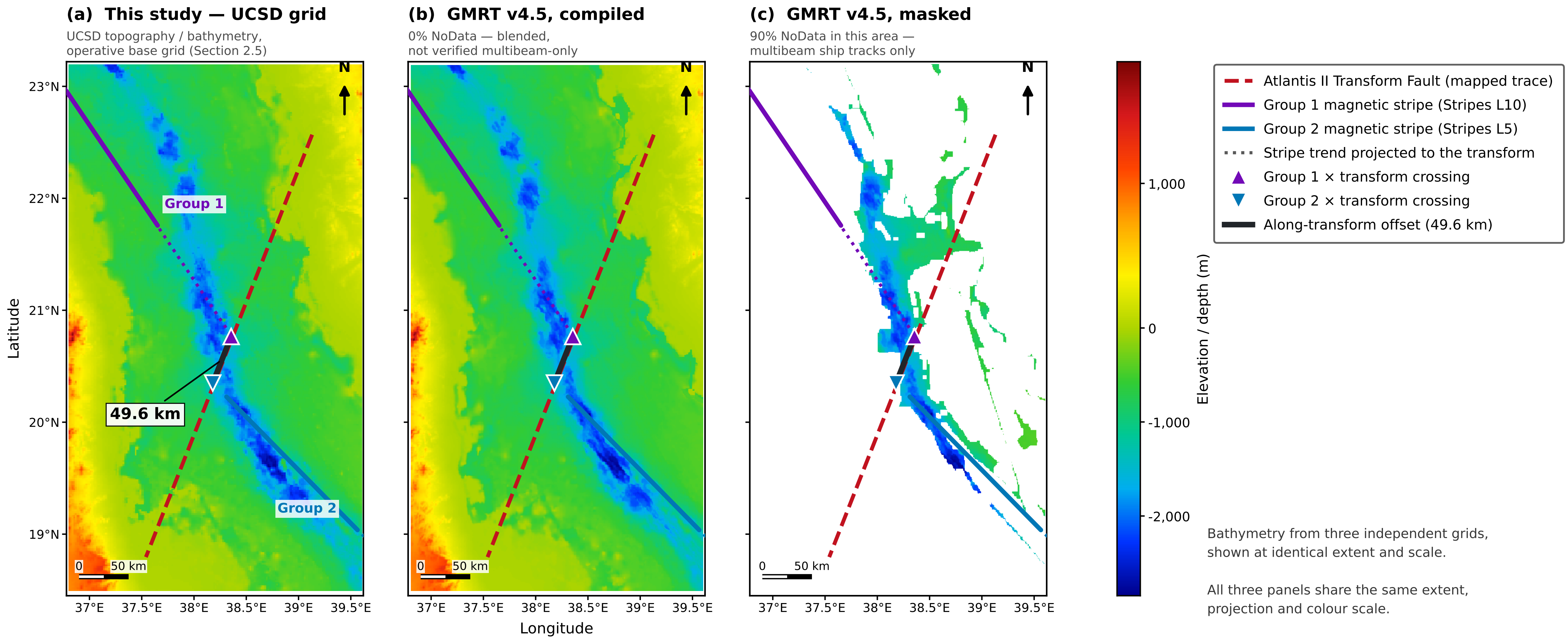

Bathymetry from three independent grids, shown at identical extent and scale.

All three panels share the same extent, projection and colour scale.

Panel (c) shows where verified multibeam coverage actually exists in this corridor.

The Atlantis II offset is measured between the crossings of the Group 1 and Group 2 stripe trends with the transform trace.

Sources: UCSD topex.ucsd.edu; GMRT v4.5 (Ryan et al., 2009).

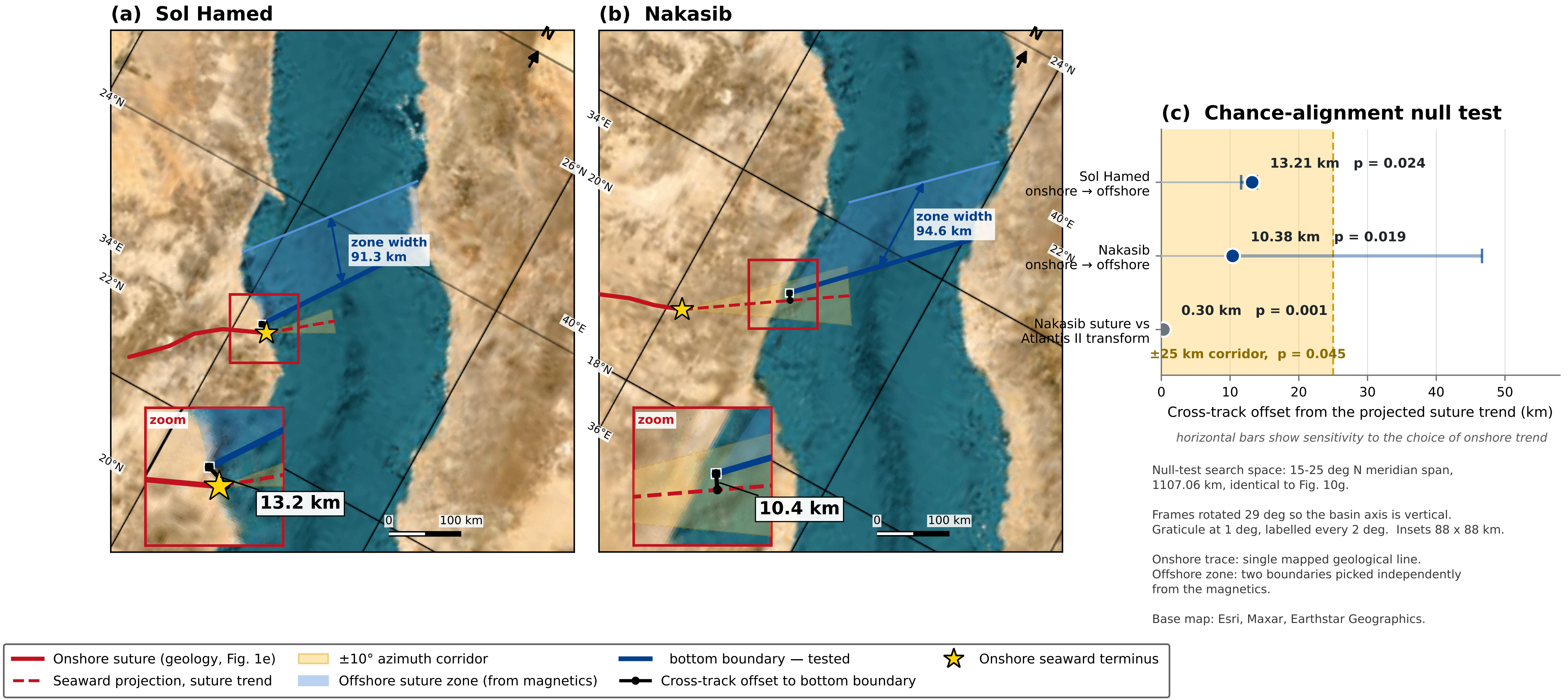
(a) Sol Hamed
(b) Nakasib
N
24°N
34°E
22°N
20°N
26°N
40°E
18°N
36°E
zone width
91.3 km
zone width
94.6 km
zoom
13.2 km
10.4 km
0
100 km
(c) Chance-alignment null test
13.21 km p = 0.024
Sol Hamed
onshore → offshore
10.38 km p = 0.019
Nakasib
onshore → offshore
0.30 km p = 0.001
Nakasib suture vs
Atlantis II transform
±25 km corridor, p = 0.045
0
10
20
30
40
50
Cross-track offset from the projected suture trend (km)
horizontal bars show sensitivity to the choice of onshore trend
Null-test search space: 15-25 deg N meridian span,
1107.06 km, identical to Fig. 10g.
Frames rotated 29 deg so the basin axis is vertical.
Graticule at 1 deg, labelled every 2 deg. Insets 88 x 88 km.
Onshore trace: single mapped geological line.
Offshore zone: two boundaries picked independently
from the magnetics.
Base map: Esri, Maxar, Earthstar Geographics.
Onshore suture (geology, Fig. 1e)
Seaward projection, suture trend
±10° azimuth corridor
Offshore suture zone (from magnetics)
bottom boundary — tested
Cross-track offset to bottom boundary
Onshore seaward terminus

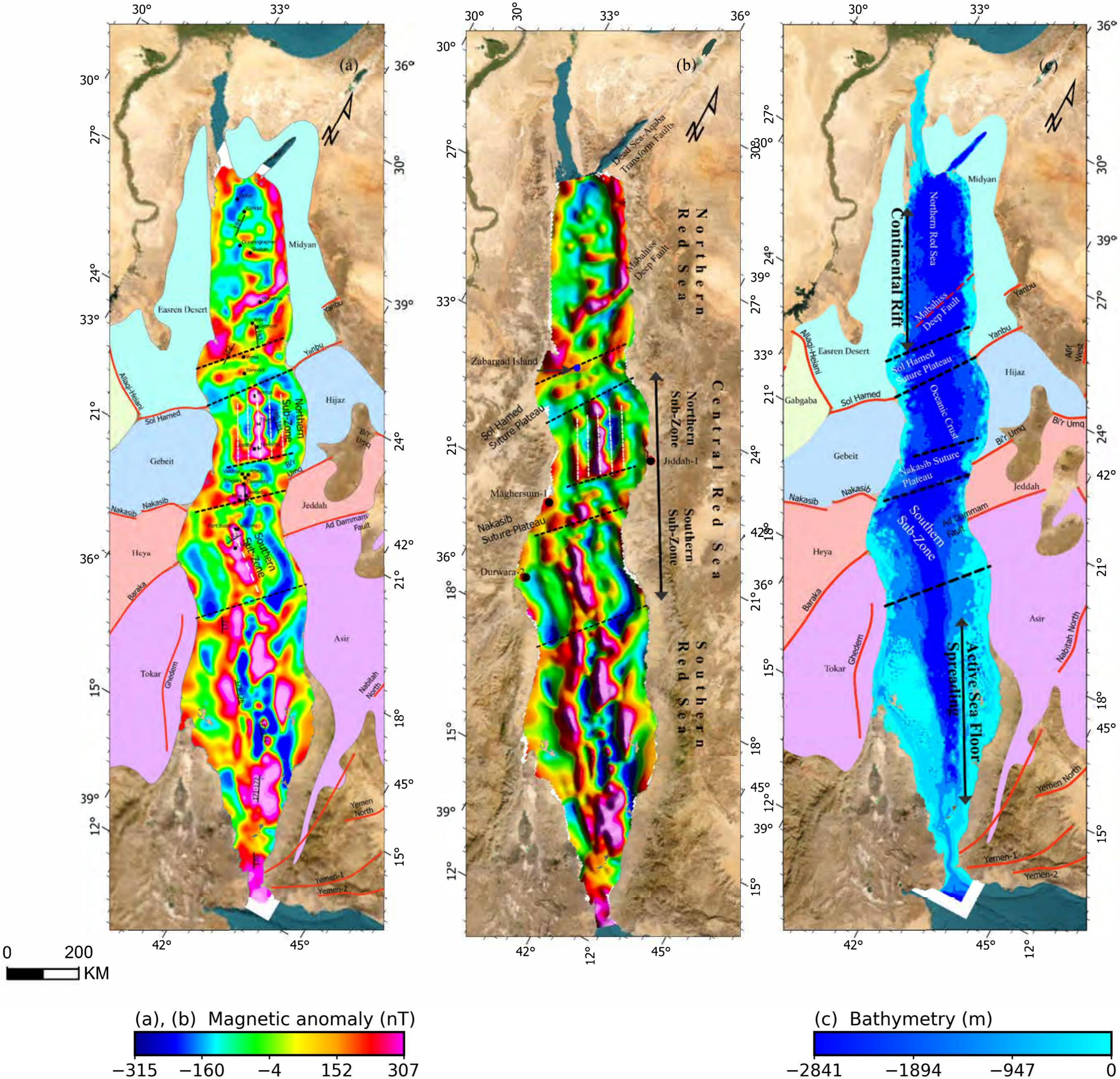
(a)
(b)
(c)
Midyan
Easren Desert
Yanbu
Hijaz
Allaqi-Heiani
Sol Hamed
Gebeit
Bi'r Umq
Nakasib
Jeddah
Ad Dammam Fault
Heya
Baraka
Asir
Tokar
Ghedem
Nabitah North
Yemen North
Yemen-1
Yemen-2
Northern Sub-Zone
Southern Sub-Zone
Dead Sea-Aqaba Transform Faults
Mabahiss Deep Fault
Northern Red Sea
Zabargad Island
Sol Hamed Suture Plateau
Jiddah-1
Maghersum-1
Nakasib Suture Plateau
Durwara-2
Central Red Sea
Southern Red Sea
Continental Rift
Oceanic Crust
Active Sea Floor Spreading
Gabgaba
Afif West
0 200 KM
(a), (b) Magnetic anomaly (nT)
−315 −160 −4 152 307
(c) Bathymetry (m)
−2841 −1894 −947 0

Alternative (non-spreading) forward models of profile A–A′ — same basement top, 3-km layer, same field parameters as the Fig. 8 spreading model